

WPPNets and WPPFlows: The Power of Wasserstein Patch Priors for Superresolution

Fabian Altekrüger^{†*} Johannes Hertrich[†]

January 6, 2023

Abstract

Exploiting image patches instead of whole images have proved to be a powerful approach to tackle various problems in image processing. Recently, Wasserstein patch priors (WPP), which are based on the comparison of the patch distributions of the unknown image and a reference image, were successfully used as data-driven regularizers in the variational formulation of superresolution. However, for each input image, this approach requires the solution of a non-convex minimization problem which is computationally costly. In this paper, we propose to learn two kind of neural networks in an unsupervised way based on WPP loss functions. First, we show how convolutional neural networks (CNNs) can be incorporated. Once the network, called WPPNet, is learned, it can be very efficiently applied to any input image. Second, we incorporate conditional normalizing flows to provide a tool for uncertainty quantification. Numerical examples demonstrate the very good performance of WPPNets for superresolution in various image classes even if the forward operator is known only approximately.

1 Introduction

In inverse problems, the task is to reconstruct an unknown ground truth \bar{x} from a noisy observation

$$y = f(\bar{x}) + \xi,$$

where f is an ill-posed forward operator and ξ is the realization of Gaussian noise with distribution $\mathcal{N}(0, \sigma^2 I)$. Such problems can be tackled by finding a minimizer of a variational problem

$$\mathcal{J}(x) = \mathcal{D}(f(x), y) + \lambda \mathcal{R}(x), \quad \lambda > 0, \quad (1)$$

where $\mathcal{D}(f(x), y)$ is a data-fidelity term which accounts for the noise and \mathcal{R} a regularizer or image prior. The concrete form of (1) is often derived by a Bayesian approach.

In this paper, we focus on the problem of superresolution. Here, \bar{x} is a high-resolution image and y a low-resolution image obtained by a forward operator f , which is usually a composition of a blur operator

*Department of Mathematics, Humboldt-Universität zu Berlin, Unter den Linden 6, D-10099 Berlin, Germany, fabian.altekrueger@hu-berlin.de

†Institute of Mathematics, Technische Universität Berlin, Straße des 17. Juni 136, D-10623 Berlin, Germany, j.hertrich@math.tu-berlin.de.

and a downsampling operator. Due to its actuality, superresolution using deep neural networks (NNs) was considered in many papers, see e.g., [15, 41, 42, 55, 56, 62, 66, 74], see also [70] for a survey. In particular, unrolled approaches like [21, 32, 45] yield good results. However, within their training process, these methods require the access to a large amount of registered pairs (\bar{x}_i, y_i) of high- and low-resolution images. Only very few NN based approaches incorporate knowledge about the forward operator f and the underlying image domain instead of large training data sets. Examples are the zero-shot superresolution [60], the deep image prior [63] and Plug-and-Play methods [65]. Zero-shot superresolution [60] exploits the internal image statistics and learns image-specific relations between the low-resolution image and its downsampled versions in order to apply these relations for reconstructing the high-resolution image. The Deep Image Prior (DIP) [63] learns a CNN by minimizing the loss function

$$\mathcal{L}_{\text{DIP}}(\theta) := \|f(G_\theta(z)) - y\|^2,$$

where z is a randomly chosen input and an early-stopping technique is used as regularization. Then, the reconstructed image is obtained by $x = G_\theta(z)$. It was shown in [63] that DIP admits competitive results for many inverse problems. In [5] a combination of DIP with the TV regularizer (DIP+TV), leading to the loss function

$$\mathcal{L}_{\text{DIP+TV}}(\theta) := \|f(G_\theta(z)) - y\|^2 + \lambda \text{TV}(G_\theta(z)), \quad \lambda > 0, \quad (2)$$

was successfully proposed for computerized tomography. Note that each reconstruction with DIP+TV requires the training of a NN, which makes the method time consuming. The idea of Plug-and-Play methods is to consider an optimization algorithm from convex analysis for solving (1), as, e.g., the forward-backward splitting [10] or the alternating direction method of multipliers [11, 16], and to replace the proximal operator with respect to the regularizer by a more general denoiser. For example, the forward backward splitting algorithm for minimizing (1) is given by

$$x_{r+1} = \text{prox}_{\eta R}(x_r - \eta \nabla_x \mathcal{D}(x_r, y))$$

and can be modified by

$$x_{r+1} = \mathcal{G}(x_r - \eta \nabla_x \mathcal{D}(x_r, y)), \quad (3)$$

where \mathcal{G} is a neural network trained for denoising natural images as the DRUNet from [71], and the hyperparameter $\eta > 0$ is the step size. Plug-and-Play methods were used for several applications in image processing with excellent performance, see e.g., [7, 22, 27, 47, 48, 71]. Closely related to Plug-and-Play methods are regularizing by denoising (RED) [54], variational networks [17] and total deep variation [36, 50].

On the other hand, powerful methods based on the self-similarity of small patches within natural images were developed in the last years. Such patch-based methods were used, e.g., for denoising [6, 29, 39, 59] and superresolution [28, 57]. In particular, the expected patch log-likelihood algorithm (EPLL) [49, 75] achieved competitive results to simple NN-based approaches by using the log-likelihood function of a Gaussian mixture model as regularizer within the variational problem (1). Recently, this approach was also extended to posterior sampling for uncertainty quantification [20].

In this paper, we assume that we are given the (approximate) forward operator $f: \mathbb{R}^{d_1 \times d_2} \rightarrow \mathbb{R}^{n_1 \times n_2}$ consisting of a blur and a downsampling operator, where $d_1 = qn_1$ and $d_2 = qn_2$ for some integral magnification factor q . Additionally, we assume that we are given a database of low-resolution images

y_1, \dots, y_m and one single high-resolution reference image \tilde{x} . Further, we assume that the distribution of patches in \tilde{x} is similar to the patch distribution in the unknown high-resolution ground truths $\bar{x}_1, \dots, \bar{x}_m$ corresponding to y_1, \dots, y_m . This assumption is fulfilled for images from similar image classes as, e.g., from textures or materials. The setting is motivated by the analysis of materials microstructures. Here, it is usually possible to scan a large area of a material with a low-resolution, while the limited amount of time and resources forbids to image the same size of a data using a higher resolution. Further, it is often impossible to scan the same section of one sample twice with different resolutions as in many applications destructive imaging processes, e.g., FIB-SEM are used. These imaging techniques destroy the scanned section of the material and consequently there is no chance to generate paired training data. Within this setting, Hertrich et al. [26] proposed to solve the variational problem (1) using a so-called Wasserstein patch prior (WPP), which penalizes the quadratic Wasserstein distance between the patch distribution of x and the reference image \tilde{x} . The approach was inspired by the idea that a texture-like image can be represented by the distribution of small patches [18, 23, 30, 31, 40], which was used by Guitierrez et al. [23] to synthesize textures and was extended by Houdard et al. [30] to generative texture modelling. Texture synthesis based on wavelet coefficients was considered in [51]. Unfortunately, the minimization of the variational problem corresponding to the WPP requires several computations and differentiations of Wasserstein distances, which is computationally expensive. We propose to overcome this computational overhead by exploiting NNs. First we introduce WPPNets, which are NNs trained in an unsupervised way using a new WPP-based loss function. Then, in order to measure the uncertainty within the reconstructions, we train conditional normalizing flows using a WPP-Kullback-Leibler-based loss function and call the resulting model WPPFlows. Normalizing flows [14, 35, 52] are learned diffeomorphisms to model complicated and high-dimensional probability distributions using a much simpler latent distribution. Applications to inverse problems were considered, e.g., in [2, 13, 61]. We demonstrate the performance of our methods by various numerical examples on real-world data¹. It turns out that WPPNets outperform several methods such as Plug-and-Play approaches and DIP. In practice, it is often unrealistic to assume that the forward operator f is known exactly. Instead, it can be described inaccurately or estimated on synthetic data. Our numerical examples show that WPPNets are much more stable under such perturbations of the operator than other approaches. Finally, our examples show that WPPFlows are a reasonable method to quantify the uncertainty within the reconstructions as they produce diverse and realistic images.

The paper is organized as follows: in Section 2, we briefly review the WPP approach from [26]. Then, in Section 3, we introduce WPPNets. Conditional normalizing flows were incorporated in Section 4 to get WPPFlows. In Section 5, we present numerical examples and compare our results with other methods. Finally, conclusions are drawn in Section 6.

2 The Wasserstein Patch Prior

Let $f: \mathbb{R}^{d_1 \times d_2} \rightarrow \mathbb{R}^{n_1 \times n_2}$ be a known forward operator with $d_1 = qn_1$ and $d_2 = qn_2$ for some integral magnification factor q . Given an observation $y = f(\bar{x}) + \xi \in \mathbb{R}^{n_1 \times n_2}$ for some noise ξ and a reference image \tilde{x} , we aim to reconstruct the unknown ground truth image $\bar{x} \in \mathbb{R}^{d_1 \times d_2}$ assuming that \bar{x} and \tilde{x} have a similar patch distribution.

For this purpose, let $P_j: \mathbb{R}^{d_1 \times d_2} \rightarrow \mathbb{R}^{s_1 \times s_2}$, $j = 1, \dots, N$ denote the operator which extracts the

¹The code is available at <https://github.com/FabianAltekrueger/WPPNets>.

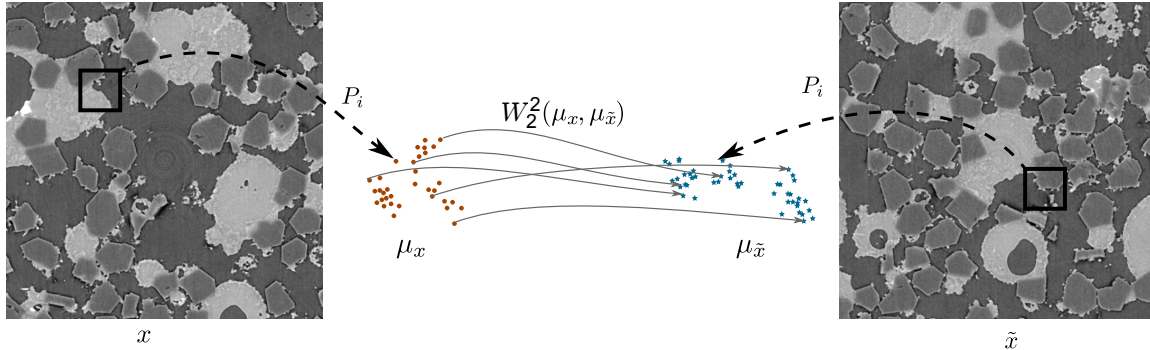


Figure 1: Visualization of the Wasserstein patch prior.

j -th patch of size $s_1 \times s_2$ with $s_1 \ll d_1$, $s_2 \ll d_2$ from an image $x \in \mathbb{R}^{d_1 \times d_2}$. Resampling the images columnwise, we may consider $f: \mathbb{R}^d \rightarrow \mathbb{R}^n$ and $P_j: \mathbb{R}^d \rightarrow \mathbb{R}^s$, where $d := d_1 d_2$, $n := n_1 n_2$ and $s := s_1 s_2$. Then we define the *empirical patch distribution* μ_x of $x \in \mathbb{R}^d$ by

$$\mu_x = \frac{1}{N} \sum_{j=1}^N \delta_{P_j(x)},$$

where δ denotes the Dirac measure. The main assumption in the following models is that similarly structured images x and \tilde{x} have also similar empirical patch distributions. Based on the empirical patch distributions of an image x and a reference image \tilde{x} , we define the *Wasserstein Patch Prior* (WPP) as the squared Wasserstein-2 distance of the corresponding empirical patch distributions, i.e.,

$$W_2^2(\mu_x, \mu_{\tilde{x}}) := \min_{\pi \in \Pi(\mu_x, \mu_{\tilde{x}})} \sum_{j=1}^N \sum_{k=1}^{\tilde{N}} \|P_j(x) - P_k(\tilde{x})\|^2 \pi_{j,k}$$

where $\Pi(\mu_x, \mu_{\tilde{x}}) := \{\pi = (\pi_{j,k}) \in \mathbb{R}_{\geq 0}^{N \times \tilde{N}} : \sum_{j=1}^N \pi_{j,k} = \frac{1}{\tilde{N}}, \sum_{k=1}^{\tilde{N}} \pi_{j,k} = \frac{1}{N}\}$. The WPP is visualized in Figure 1. Note that it is not required that the images have the same size. Instead, we only require that all patches have the same size. We will frequently use the semi-dual form of the Wasserstein distance, see e.g., [58, Chapter 1],

$$W_2^2(\mu_x, \mu_{\tilde{x}}) = \max_{\psi \in \mathbb{R}^{\tilde{N}}} \left(\frac{1}{N} \sum_{j=1}^N \psi^c(P_j(x)) + \frac{1}{\tilde{N}} \sum_{k=1}^{\tilde{N}} \psi_k \right), \quad (4)$$

where $\psi := (\psi_k)_{k=1}^{\tilde{N}}$ and $\psi^c(P_j(x)) := \min_{k \in \{1, \dots, \tilde{N}\}} \{\|P_j(x) - P_k(\tilde{x})\|^2 - \psi_k\}$ denotes the c -transform of ψ . In [26], the WPP is used as regularizer in the variational problem

$$\mathcal{J}(x) := \frac{1}{2} \|f(x) - y\|^2 + \lambda W_2^2(\mu_x, \mu_{\tilde{x}}). \quad (5)$$

It was shown that (5) outperforms state-of-the-art methods for superresolution of material images. However, it requires the minimization of the functional (5) for each high-resolution image x we want to reconstruct from its low-resolution counterpart, which is computationally costly. Therefore, in the next

section we propose to learn a NN based on the above loss function and then to use this network to generate high-resolution images in a fast way.

3 WPPNets

We assume that we are given a high-resolution reference image $\tilde{x} \in \mathbb{R}^d$ and several low-resolution images $y_i \in \mathbb{R}^n$, $i = 1, \dots, m$, $n < d$. The corresponding high-resolution ground truth images $\bar{x}_i \in \mathbb{R}^d$, $i = 1, \dots, m$ are unknown, but we assume that the patch distributions within the reference image \tilde{x} and the ground truths \bar{x}_i are similar. Based on (5) it appears natural to train a CNN $G_\theta: \mathbb{R}^n \rightarrow \mathbb{R}^d$ using the loss function

$$\mathcal{L}(\theta) := \frac{1}{m} \sum_{i=1}^m \|f(G_\theta(y_i)) - y_i\|^2 + \lambda W_2^2(\mu_{G_\theta(y_i)}, \mu_{\tilde{x}}). \quad (6)$$

In other words, the network will be trained to map an observation y onto the corresponding WPP reconstruction x , which is the minimizer of (5). As the CNN G_θ is fully convolutional, we can apply it for images of arbitrary size. More precisely, G_θ maps a low-dimensional input image of size $n_1 \times n_2$ to a high-resolution image of size $d_1 \times d_2$ with $d_1 = qn_1$ and $d_2 = qn_2$, where q is the magnification factor.

Since each training image shows only a small part of the considered texture or material, the patch distribution in this part might have a severe bias compared with the patch distribution in the whole texture or material because of local structures shown in this specific part. Consequently, the Wasserstein patch prior, which enforces equality of these patch distributions, does not make sense when it is applied on too small images. As a remedy, we divide our training data into disjoint batches $(B_j)_j$ of size $|B_j| = b$, $j = 1, \dots, N_B$ with $\bigcup_{j=1}^{N_B} B_j = \{1, \dots, m\}$. Then the loss function (6) can be rewritten to

$$\mathcal{L}(\theta) = \frac{1}{N_B} \sum_{j=1}^{N_B} \left(\frac{1}{b} \sum_{i \in B_j} \|f(G_\theta(y_i)) - y_i\|^2 + \lambda \frac{1}{b} \sum_{i \in B_j} W_2^2(\mu_{G_\theta(y_i)}, \mu_{\tilde{x}}) \right). \quad (7)$$

Instead of comparing the patch distributions of \tilde{x} and $G_\theta(y_i)$ by $W_2^2(\mu_{G_\theta(y_i)}, \mu_{\tilde{x}})$ for each i separately, we now compare the patch distribution of \tilde{x} with the distribution of all patches within the images of the batch B_j . This can be seen as a concatenation of the reconstructed images $G_\theta(y_i)$, $i \in B_j$ for some batch B_j , in order to reduce the bias of the patch distribution of the single reconstructions $G_\theta(y_i)$ compared to the patch distribution of all reconstructions. Formally, this corresponds to replacing in (7) the term

$$\frac{1}{b} \sum_{i \in B_j} W_2^2(\mu_{G_\theta(y_i)}, \mu_{\tilde{x}}) \quad \text{by} \quad W_2^2\left(\frac{1}{b} \sum_{i \in B_j} \mu_{G_\theta(y_i)}, \mu_{\tilde{x}}\right),$$

for $j = 1, \dots, N_B$. Then, we obtain the loss function

$$\mathcal{L}_{\text{WPPNet}}(\theta) := \frac{1}{N_B} \sum_{j=1}^{N_B} \left(\frac{1}{b} \sum_{i \in B_j} \|f(G_\theta(y_i)) - y_i\|^2 + \lambda W_2^2\left(\frac{1}{b} \sum_{i \in B_j} \mu_{G_\theta(y_i)}, \mu_{\tilde{x}}\right) \right). \quad (8)$$

We call a neural network trained with the loss function (8) a *Wasserstein Patch Prior Network* (WPPNet).

Remark 1. *The required batch size depends on the size of the low-resolution example images y_i , $i =$*

1, ..., m and on the level of homogeneity of the considered texture or material. In the case of large example images y_i and a very homogeneous texture, we can assume that the patch distribution in each image y_i is representative for the whole texture. Consequently, we can choose batch size $b = 1$. In this case, the loss functions (8) and (7) coincide. However, in practice, we have often only access to small low-resolution images and in particular for applications with materials' microstructures the considered images admit a lower homogeneity such that larger batch sizes are necessary.

In order to minimize the loss function (8) with a gradient-based optimization method, we need to compute the derivative of $W_2^2(\mu_{G_\theta(y)}, \mu_{\tilde{x}})$ with respect to θ for some observation $y \in \mathcal{Y}$.

Since the Wasserstein distance is computed iteratively, the application of backpropagation is computationally intractable. Instead, we compute the derivative via the semi-dual formulation of the Wasserstein distance. To this end, recall that the Wasserstein distance reads in its semi-dual form as

$$W_2^2(\mu_{G_\theta(y)}, \mu_{\tilde{x}}) = \max_{\psi \in \mathbb{R}^{\tilde{N}}} F(\psi, \theta; y), \quad F(\psi, \theta; y) := \frac{1}{N} \sum_{j=1}^N \psi^c(P_j(G_\theta(y))) + \frac{1}{\tilde{N}} \sum_{k=1}^{\tilde{N}} \psi_k.$$

Then the following well-known theorem provides a connection between the gradient of the Wasserstein distance and those of F , see e.g., [30].

Theorem 2. *Let both $\theta \mapsto W_2^2\left(\frac{1}{N} \sum_{j=1}^N \delta_{P_j(G_\theta(y))}, \frac{1}{\tilde{N}} \sum_{k=1}^{\tilde{N}} \delta_{P_k(\tilde{x})}\right)$ and $\theta \mapsto F(\psi^*, \theta; y)$ be differentiable at θ_0 with $\psi^* \in \arg \max_{\psi} F(\psi, \theta_0; y)$. Then it holds*

$$\nabla_{\theta} W_2^2\left(\frac{1}{N} \sum_{j=1}^N \delta_{P_j(G_{\theta_0}(y))}, \frac{1}{\tilde{N}} \sum_{k=1}^{\tilde{N}} \delta_{P_k(\tilde{x})}\right) = \nabla_{\theta} F(\psi^*, \theta_0; y).$$

Since for almost every θ the set of minimizers

$$\kappa_{\psi}(j) = \arg \min_{k \in \{1, \dots, \tilde{N}\}} (\|P_j(G_{\theta}(y)) - P_k(\tilde{x})\|^2 - \psi_k) \quad (9)$$

is single-valued, it holds that $\psi^c(P_j(G_{\theta}(y))) = \|P_j(G_{\theta}(y)) - P_{\kappa_{\psi}(j)}(\tilde{x})\|^2 - \psi_{\kappa_{\psi}(j)}$, which is differentiable in θ if G_{θ} is. Thus, by Theorem 2, the gradient of the Wasserstein distance is given by

$$\begin{aligned} \nabla_{\theta} W_2^2(\mu_{G_{\theta}(y)}, \mu_{\tilde{x}}) &= \nabla_{\theta} F(\psi^*, \theta; y) \\ &= \frac{2}{N} \sum_{j=1}^N \left(\partial_{\theta} (P_j(G_{\theta}(y)))^T \right) \left(P_j(G_{\theta}(y)) - P_{\kappa_{\psi^*}(j)}(\tilde{x}) \right), \end{aligned}$$

where $\psi^* := \arg \max_{\psi \in \mathbb{R}^{\tilde{N}}} F(\psi, \theta; y)$. For computing ψ^* , we use a (stochastic) gradient ascent algorithm as suggested in [30].

Remark 3 (Computational Complexity). *The computation of (the gradient of) $W_2^2(\mu_{G_{\theta}(y)}, \mu_{\tilde{x}})$ does not scale well with the number of patches N and \tilde{N} of the reconstruction $G_{\theta}(y)$ and the reference image \tilde{x} . More precisely, it has complexity $\mathcal{O}(N\tilde{N})$ due to the computation of the κ_{ψ} in (9). As both N and \tilde{N} might be large, this leads to an intractable computational effort. To speed up the numerical computations, we replace the empirical patch distribution $\mu_{\tilde{x}}$ by the distribution of a random subset of all patches, i.e.,*

we redefine $\mu_{\tilde{x}}$ as

$$\mu_{\tilde{x}} = \frac{1}{|I|} \sum_{k \in I} \delta_{P_k(\tilde{x})},$$

where I is a random subset of $\{1, \dots, \tilde{N}\}$ of size $|I| \ll \tilde{N}$. Since $\mu_{\tilde{x}}$ has to be a fixed measure, this set I is chosen once in the beginning and kept over the whole training procedure. Then, the complexity of the computation of (the gradient of) $W_2^2(\mu_{G_\theta(y)}, \mu_{\tilde{x}})$ reduces to $\mathcal{O}(N|I|)$. Note that we cannot subsample the patch distribution of the reconstruction in the same way as this would lead to pixels in the reconstructions, which are not effected by the regularizer. For our numerical experiments we chose $|I| = 10000$.

Remark 4 (Relation to the deep image prior). *In the case that $m = 1$, i.e., when we have given exactly one training image, the loss function of the WPPNet reads as*

$$\|f(G_\theta(y)) - y\|^2 + \lambda W_2^2(\mu_{G_\theta(y)}, \mu_{\tilde{x}}).$$

This is quite similar to the loss function of DIP+TV (2) with the only difference that the TV regularization is replaced by a WPP regularizer. Consequently, in this case, we can interpret the WPPNet as deep image prior with WPP regularization. However, it is well known that the reconstructions of the deep image prior are highly adapted to the considered observation and do not generalize to observations which are unseen during the training time. Therefore, this relation of WPPNets to the deep image prior holds not longer true as soon as the number m of low-resolution images is larger than 1. Nevertheless, we can hope that the effect of a “regularization by a CNN architecture” improves the results of the WPPNet over the variational WPP reconstruction in some cases.

4 WPPFlows

For several applications, it is crucial to get not only a realistic reconstruction x , but also to measure the uncertainty within the reconstruction. From a mathematical point of view this corresponds to reconstructing the full posterior distribution $P_{X|Y=y}$ within the Bayesian inverse problem

$$Y = f(X) + \Xi, \tag{10}$$

where $\Xi \sim \mathcal{N}(0, \sigma^2 I)$ is independent of X , For this purpose, we will make use of *conditional normalizing flows*. In particular, this allows to produce different possible high-resolution reconstructions from the same low-resolution image y .

Within the Bayesian inverse problem (10) we need to specify the prior distribution P_X . Here, we assume that it is defined via the Wasserstein patch prior by the density

$$p_X(x) \sim \exp(-\rho W_2^2(\mu_x, \mu_{\tilde{x}})), \tag{11}$$

where $\rho > 0$ is a hyperparameter. The following proposition ensures that this defines indeed a probability distribution, which is crucial to apply the concepts from Bayesian statistics.

Proposition 5. *The function $\varphi(x) := \exp(-\rho W_2^2(\mu_x, \mu_{\tilde{x}}))$ is integrable.*

The proof is given in Appendix A.

The following remark interprets the variational WPP model (5) from the previous sections as maximum-a-posteriori estimator (MAP) within the Bayesian inverse problem (10).

Remark 6. *Under the assumption that $P_{Y|X=x} = \mathcal{N}(f(x), \sigma^2 I)$, Bayes' theorem implies that maximizing the log-posterior distribution $\log(p_{X|Y=y}(x))$ corresponding to (10) can be written as*

$$\begin{aligned} \arg \max_x \{\log(p_{X|Y=y}(x))\} &= \arg \max_x \left\{ \log \left(\frac{p_{Y|X=x}(y) p_X(x)}{p_Y(y)} \right) \right\} \\ &= \arg \max_x \left\{ \log \left(\exp(-\|f(x) - y\|^2 / (2\sigma^2)) \right) + \log(p_X(x)) \right\} \\ &= \arg \min_x \left\{ \frac{1}{2} \|f(x) - y\|^2 - \sigma^2 \log(p_X(x)) \right\}. \end{aligned}$$

For the prior (11) with $\rho := \frac{\lambda}{\sigma^2}$ this gives the variational WPP model (5).

Normalizing Flows The aim of normalizing flows is to sample from a complicated probability distribution P_X which admits the density function p_X . A *normalizing flow* $\mathcal{T} = \mathcal{T}_\theta: \mathbb{R}^d \rightarrow \mathbb{R}^d$ is an invertible neural network with parameters θ , which is learned to push forward a simple distribution P_Z (usually a standard Gaussian) to P_X such that $\mathcal{T}_\# P_Z = P_Z \circ \mathcal{T}^{-1} \approx P_X$. Here, the symbol \approx means that the distributions are similar in some proper distance or divergence. Several architectures of normalizing flows were proposed in literature [8, 19, 35, 52]. Here, we use an adaption of the SRFlow architecture [44] based on affine coupling blocks [4, 14]. A detailed description is given in Appendix C.

For applications in inverse problems, normalizing flows were generalized to incorporate a condition [3, 25]. More precisely, for approximating all posterior distributions $P_{X|Y=y}$ within the Bayesian inverse problem (10) using a flow model, we learn a mapping $\mathcal{T} = \mathcal{T}_\theta: \mathbb{R}^d \times \mathbb{R}^n \rightarrow \mathbb{R}^d$ such that for all $y \in \mathbb{R}^n$ we have that $\mathcal{T}(\cdot, y)$ is invertible and that $\mathcal{T}(\cdot, y)_\# P_Z \approx P_{X|Y=y}$. Note, that (conditional) normalizing flows can be generalized for the use of non-deterministic transformation, see the overview paper [24].

To ensure $\mathcal{T}(\cdot, y)_\# P_Z \approx P_{X|Y=y}$, we use the expectation on Y of the *backward Kullback-Leibler (KL) divergence*

$$\mathcal{L}(\theta) := \mathbb{E}_{y \sim P_Y} [\text{KL}(\mathcal{T}(\cdot, y)_\# P_Z, P_{X|Y=y})] \quad (12)$$

This was also proposed in [2, 25, 37, 61]. The KL divergence is not symmetric and for a discussion on forward versus backward Kullback-Leibler divergences we refer to [25].

For computing \mathcal{L}_θ and taking its derivative, we use the following proposition, which is a combination of [2, Prop. 1] and [4].

Proposition 7. *Let X and Y be related by the Bayesian inverse problem (10). Then, for any $y \in \mathbb{R}^n$, the KL divergence $\text{KL}(\mathcal{T}(\cdot, y)_\# P_Z, P_{X|Y=y})$ is up to a constant equal to*

$$\mathbb{E}_{z \sim P_Z} \left[\frac{1}{2\sigma^2} \|f(\mathcal{T}(z, y)) - y\|^2 + \log(p_X(\mathcal{T}(z, y))) - \log(|\det(\nabla \mathcal{T}(z, y))|) \right]$$

By discretizing the expectation of P_Y by independent samples y_1, \dots, y_m of Y and using our definition

(11) of the prior distribution p_X , we obtain by Proposition 7 that the loss function from (12) is given by

$$\mathcal{L}(\theta) \cong \frac{1}{m} \sum_{i=1}^m \mathbb{E}_{z \sim P_Z} \left[\frac{1}{2\sigma^2} \|f(\mathcal{T}(z; y_i)) - y_i\|^2 + \rho W_2^2(\mu_{\mathcal{T}(z; y_i)}, \mu_{\bar{x}}) - \log |\det \nabla \mathcal{T}(z; y_i)| \right],$$

where the symbol \cong indicates equality up to a constant. As in Section 3, we merge the patch distribution of a batch of images such that we obtain the loss function

$$\mathcal{L}_{\text{WPPFlow}}(\theta) := \mathbb{E}_{z_1, \dots, z_m \sim (P_Z)^m} \left[\frac{1}{|B|} \sum_{j=1}^{N_B} \frac{1}{b} \sum_{i \in B_j} \frac{\|f(\mathcal{T}(z_i; y_i)) - y_i\|^2}{2\sigma^2} - \log |\det \nabla \mathcal{T}(z_i; y_i)| + \rho W_2^2\left(\frac{1}{b} \sum_{i \in B_j} \mu_{\mathcal{T}(z_i; y_i)}, \mu_{\bar{x}}\right) \right].$$

We call a normalizing flow trained by this loss function *Wasserstein Patch Prior Flow* (WPPFlow).

Remark 8 (MCMC methods). *Using Bayes formula, we can evaluate the density of the log-posterior distribution up to a constant by*

$$\begin{aligned} \log(p_{X|Y=y}(x)) &\cong \log(p_{Y|X=x}(y)) \log(p_X(x)) \\ &\cong -\frac{1}{2\sigma^2} \|f(x) - y\|^2 - \rho W_2^2(\mu_x, \mu_{\bar{x}}). \end{aligned} \tag{13}$$

A classical possibility for sampling from a probability distribution whose density is known up to a constant are Markov chain Monte Carlo (MCMC) methods like the Metropolis Hastings algorithm or the Langevin dynamics, see [53] for an overview. However, the methods do not scale very well in high dimensions and for images usually several millions of evaluations of the target density are required. This makes the application of MCMC methods impossible when the evaluation of the target density is costly. In our case the posterior density (13) includes the computation of the Wasserstein distance of the empirical patch distributions. Even though there exist efficient algorithms for computing Wasserstein distances, such a large number of evaluations leads to an intractable computational effort. For a detailed comparison of MCMC methods and normalizing flows on a smaller problem, we refer to [2].

5 Numerical Results

In this section we demonstrate the good performance of our methods. In Subsection 5.1 and 5.2, we assume that the forward operator f , consisting of a blur operator and a downsampling operator, is given exactly. Then, in Subsection 5.3, we demonstrate the robustness of WPPNets by assuming that the operator knowledge is inaccurate. In the first example, we generate the low-resolution data by a slightly different operator than we use for learning the WPPNet. In the second example, we consider real data, where the forward operator f is unknown. We estimate the forward operator f based on one pair of registered images and we use this (inaccurate) estimation of the operator for superresolution. Finally, in Subsection 5.4 we consider the uncertainty in reconstructing from a low-resolution image using WPPFlows. Details on the architecture and the experimental setup are given in Appendix B.

We compare our WPPNet with the following methods:

- **bicubic interpolation** [33].
- **Plug-and-Play Forward Backward Splitting with DRUNet** (PnP-DRUNet): we use the DRUNet from [71] as denoiser \mathcal{G} in (3) and run 100 iterations. Even with the learned NN, PnP-DRUNet is significantly slower than a simple evaluation of the WPPNet.
- **Deep Image Prior with TV regularization** (DIP+TV) [63]²: note that each reconstruction with the DIP+TV requires the training of a neural network. Thus, the reconstruction time of DIP+TV is much slower than for the WPPNet.
- **ACNN** trained on natural images: a natural way to overcome the issue of missing (paired) training data could be to train a CNN onto natural images and to hope that it generalizes to the special structured test set. Following this approach, we compare our results with an asymmetric CNN (ACNN) [62] trained on the 400 training images from the BSDS500 dataset [46]. As loss function, we use the standard L^2 -loss. Afterwards we apply these networks to our special structured test set. Training and reconstruction time of a ACNN is comparable with those of a WPPNet. Note that the architecture we use here is the same as for the WPPNet.
- **WPP** from (5).

We compare the WPPFlow with the following method:

- **SRFlow** trained on natural images: we train a modified version of the SRFlow [44]. The loss function used in [44] is the negative log-likelihood which is equivalent to interchanging the two arguments in the loss function (12). Note that this leads to a loss function which requires a large database of paired training data. As we assume that such a database is not available, we use the DIV2K images [1] as training images. Note that the architecture we use here is the same as for the WPPFlow.

We have to emphasize that, except the WPP, these methods do not include some prior information and thus have some weaker assumptions than WPPNets. Nevertheless, there are not many comparison methods which include only one high-resolution image. The intention is to demonstrate the impact of including a comparably small knowledge about the underlying image domain.

To evaluate the quality of our results, we use different quality measures:

- **PSNR**. For two images x and y on $[0, 1]^{m \times n}$, the peak-signal to noise ration is defined as

$$\text{PSNR}(x, y) = -10 \log_{10} \left(\frac{1}{mn} \|x - y\|^2 \right).$$

Larger PSNR values correspond to a better reconstruction. It is well-known that the PSNR prefers very smooth reconstructions which does in general not coincide with the visual impression.

- **Blur effect** [12]. This metric is based on comparing an input image x with a blurred version x_{blur} . For sharp images x , the difference should be very pronounced while it will be small for blurred x . The blur effect is normalized to $[0, 1]$, where a small blur effect indicates that x is very sharp while a large blur effect means that x is very blurry.

²We use the original implementation from [63] available at <https://github.com/DmitryUlyanov/deep-image-prior>

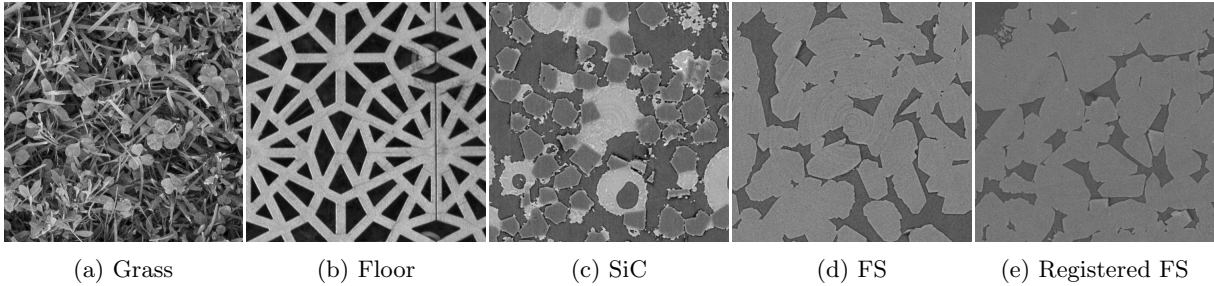


Figure 2: Reference images used for the numerical examples.

- **LPIPS** [73]³. The basic idea of the learned perceptual image patch similarity is to compare the feature maps extracted from some deep neural network that is trained for some classical imaging task which is not necessarily related to our original problem. A small value of LPIPS indicates a high perceptual similarity.
- **SSIM** [69]. The structural similarity index measure compares the overall image structure of two images x and y on $[0, 1]^{n \times n}$. It is computed by moving a local window at M locations

$$\text{SSIM}(x, y) := \frac{1}{M} \sum_{i=1}^M \frac{(2\mu_x^{(i)}\mu_y^{(i)} + C_1)(2\sigma_{xy}^{(i)} + C_2)}{((\mu_x^{(i)})^2 + (\mu_y^{(i)})^2 + C_1)((\sigma_x^{(i)})^2 + (\sigma_y^{(i)})^2 + C_2)},$$

where $\mu_x^{(i)}$ and $\mu_y^{(i)}$ are the mean intensity, $\sigma_x^{(i)}$ and $\sigma_y^{(i)}$ are the standard deviation and $\sigma_{xy}^{(i)}$ is the covariance of x and y at the local window i . The local window is chosen to be 7×7 and the constants $C_1 = (K_1 L)^2$, $C_2 = (K_2 L)^2$ ensure stability, where $K_1 = 0.01$, $K_2 = 0.03$ and $L = \max(x) - \max(y)$ is the data range as in [69].

- **FSIM** [72]. The basic idea of the feature-based similarity index (FSIM) is not to compare the raw pixel values, but to compare the similarity of certain feature maps extracted from the images. We use the same feature maps as in the original paper [72].

Since we do not want to consider boundary effects, we do not consider a boundary of 40 pixels when evaluating the quality measures. All figures show the full images and zoom-in parts below them.

5.1 Texture Superresolution

First, we consider the Kylberg texture dataset [38]⁴. Here, we use the textures “Grass” and “Floor”. The high-resolution ground truth and the reference image are different 600×600 sections cropped from the original texture images, see Figures 2a and 2b. Similarly, the low-resolution training data is generated by cropping 100×100 sections from the texture images and artificially downsampling it by a predefined forward operator f . The forward operator f is a convolution with a 16×16 Gaussian blur kernel with standard deviation 2, stride 4 and $\xi \sim \mathcal{N}(0, 0.01^2)$ is some noise. Note that the stride determines the subsampling factor in each direction. To keep the dimensions consistent, we use zero-padding. As weighting parameter in the WPP-loss (8) we used $\lambda = 12.5$.⁵

³We use the implementation <https://github.com/richzhang/PerceptualSimilarity>, version 0.1.

⁴available at <https://kylberg.org/kylberg-texture-dataset-v-1-0>

⁵The implementation of this example is available online at <https://github.com/FabianAltekrueger/WPPNets>.

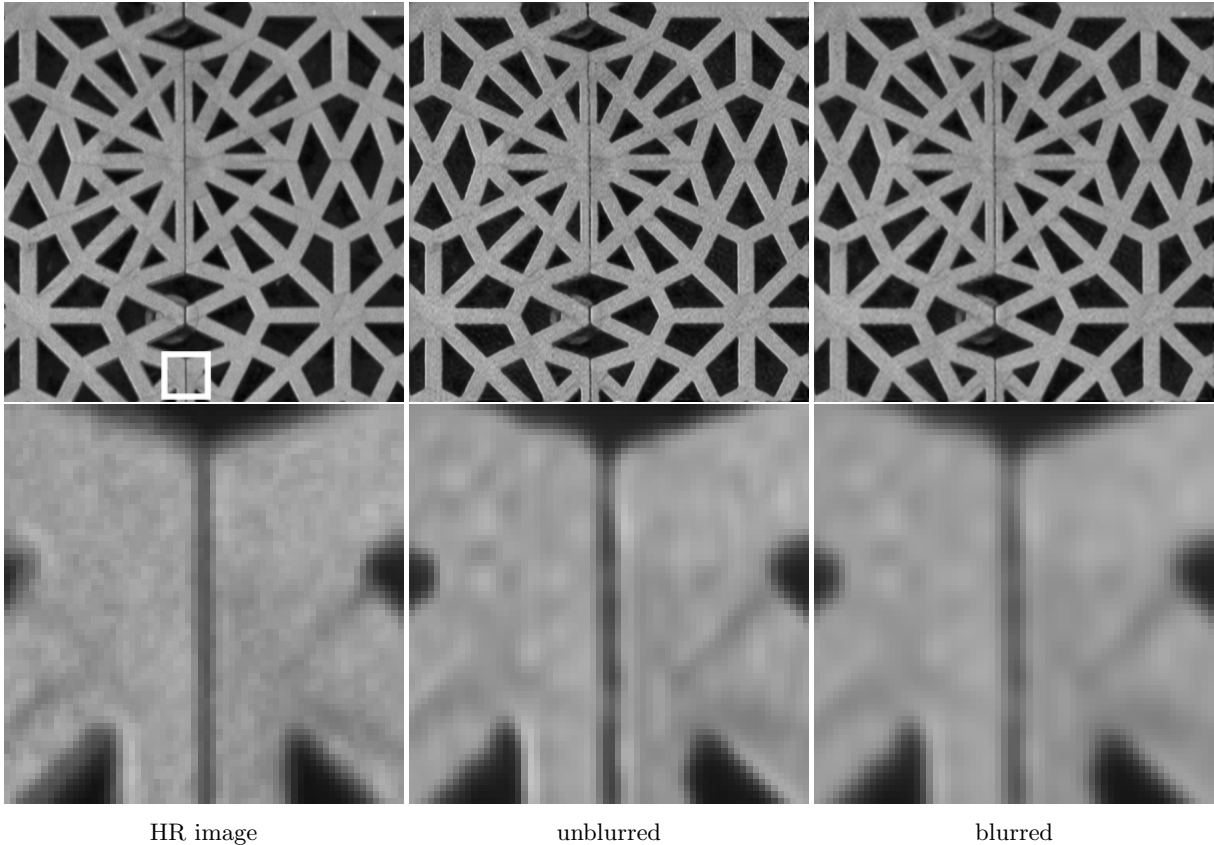


Figure 3: Comparison of unblurred and blurred WPPNet reconstruction. The zoomed-in part is marked with a white box in the HR image.

The resulting quality measures are given in Table 1 and the reconstructions are shown in Figure 4 and 5, respectively. We observe that the WPPNet and WPP lead to significantly sharper and visually better results than the other methods. However, the WPP requires the minimization of the functional (5) for each reconstruction, which is computationally costly. Also DIP+TV requires for any reconstruction the training of a NN and for PnP-DRUNet, we have to compute the iteration (3) several times. Thus, the reconstruction time for WPP, DIP+TV and PnP-DRUNet is significantly larger than for WPPNet and ACNN.

Further, we observe that PnP-DRUNet and DIP+TV have a better PSNR value than the WPPNet for the texture “Floor”. However, it is well-known that the PSNR as quality measure prefers smooth images. In terms of the blur effect, LPIPS, FSIM and the visual impression, the WPPNet and WPP are clearly better than the other methods. Considering the results, we can see that PnP-DRUNet, DIP+TV and ACNN tend to generate oversmoothed images, while WPP and WPPNet tend to oversharpen the reconstruction. This hypothesis can be underlined, by the fact that the PSNR and SSIM values of the WPPNet reconstruction can be significantly improved by applying a Gaussian blur filter with standard deviation 0.7 for grass and 1.0 for floor on the reconstruction, see Table 1 (right).

Within the WPPNet reconstruction of the “Grass” texture, we observe slightly structured noise. This can be explained by the fact that the reference image is very noisy, see Figure 2a.

⁶For the PnP-DRUNet we used a pretrained denoiser.

		bicubic	PnP-DRUNet	DIP+TV	ACNN	WPP	WPPNet	WPPNet blur
Grass	PSNR	22.68	24.71	24.97	25.06	24.61	24.79	24.95
	Blur Effect	0.5980	0.4649	0.4410	0.4307	0.4153	0.4219	0.4495
	LPIPS	0.4891	0.4074	0.2287	0.2403	0.1777	0.2353	0.2729
	SSIM	0.6442	0.7529	0.7626	0.7683	0.7473	0.7581	0.7602
	FSIM	0.8820	0.9188	0.9364	0.9328	0.9420	0.9378	0.9340
Time	Training	-	-	-	3h	-	8h	
	Reconstruction	0.0003s	51.36s	114.42s	0.05s	477.06s	0.05s	
Floor	PSNR	29.03	32.96	32.90	30.35	30.39	30.99	32.86
	Blur Effect	0.7469	0.6803	0.6690	0.5977	0.5218	0.5407	0.6187
	LPIPS	0.2568	0.2584	0.2462	0.2795	0.1647	0.1705	0.1800
	SSIM	0.8091	0.8552	0.8507	0.8345	0.7850	0.7969	0.8413
	FSIM	0.9435	0.9773	0.9776	0.9722	0.9752	0.9796	0.9878
Time	Training	-	-	-	3h	-	9.5h	
	Reconstruction	0.0003s	51.36s	114.42s	0.05s	477.06s	0.05s	

Table 1: Comparison of superresolution results for the textures “Grass” and “Floor” (stride 4). The best two values are marked in bold, the best one is additionally underlined.

5.2 Synchrotron Computed Tomography Data

Next we consider material data which was also used in [26, 28]. A series of multi-scale 3D images has been acquired by synchrotron micro-computed tomography at the SLS beamline TOMCAT. Samples of two materials were selected to provide 3D images having different levels of complexity, namely

- “SiC Diamonds” obtained by microwave sintering of silicon and diamonds, see [64].
- “FS” (Fontainebleau sandstone), a rather homogeneous natural rock that is commonly used in the oil industry for flow experiments.

In our experiments we consider a voxel spacing of 1.625 μm . From this 3D image we extract 2D slices of size 600×600 and use them as ground truth and reference images for our experiments, see Figures 2c and 2d. Since we require that the forward operator f is known (same f as in Section 5.1), we generate the low-resolution images artificially by extracting 2D slices from our 3D image and downsample it using the known predefined forward operator f . In this way, we generate a set of 1000 low-resolution images of size 25×25 for training the WPPNet.

The resulting quality measures are given in Table 2 and the reconstructions are shown in Figure 6 and 7. Similar as in Subsection 5.1, we observe that the reconstructions with WPPNet and WPP are significantly sharper and visually better than the other methods. Again, the PSNR prefers in some cases the much smoother reconstructions of DIP+TV and ACNN. However, the results of WPPNet and WPP look visually much better which is also quantified by smaller values for LPIPS, FSIM and blur effect.

We apply all methods onto a larger test set in Appendix D.

Higher Magnification Factor Additionally to the previous examples, we apply WPPNets for super-resolution with a magnification factor of 6 onto the SiC Diamonds image. Here, the forward operator f is given by a convolution with a 16×16 Gaussian blur kernel with standard deviation 3, stride 6 and zero-padding. As before, we set the noise to $\xi \sim \mathcal{N}(0, 0.01^2)$. We use the same ground truth and reference image as before, illustrated in Figure 2. The resulting quality measures are given in Table 3 and the reconstructions are shown in Figure 8.

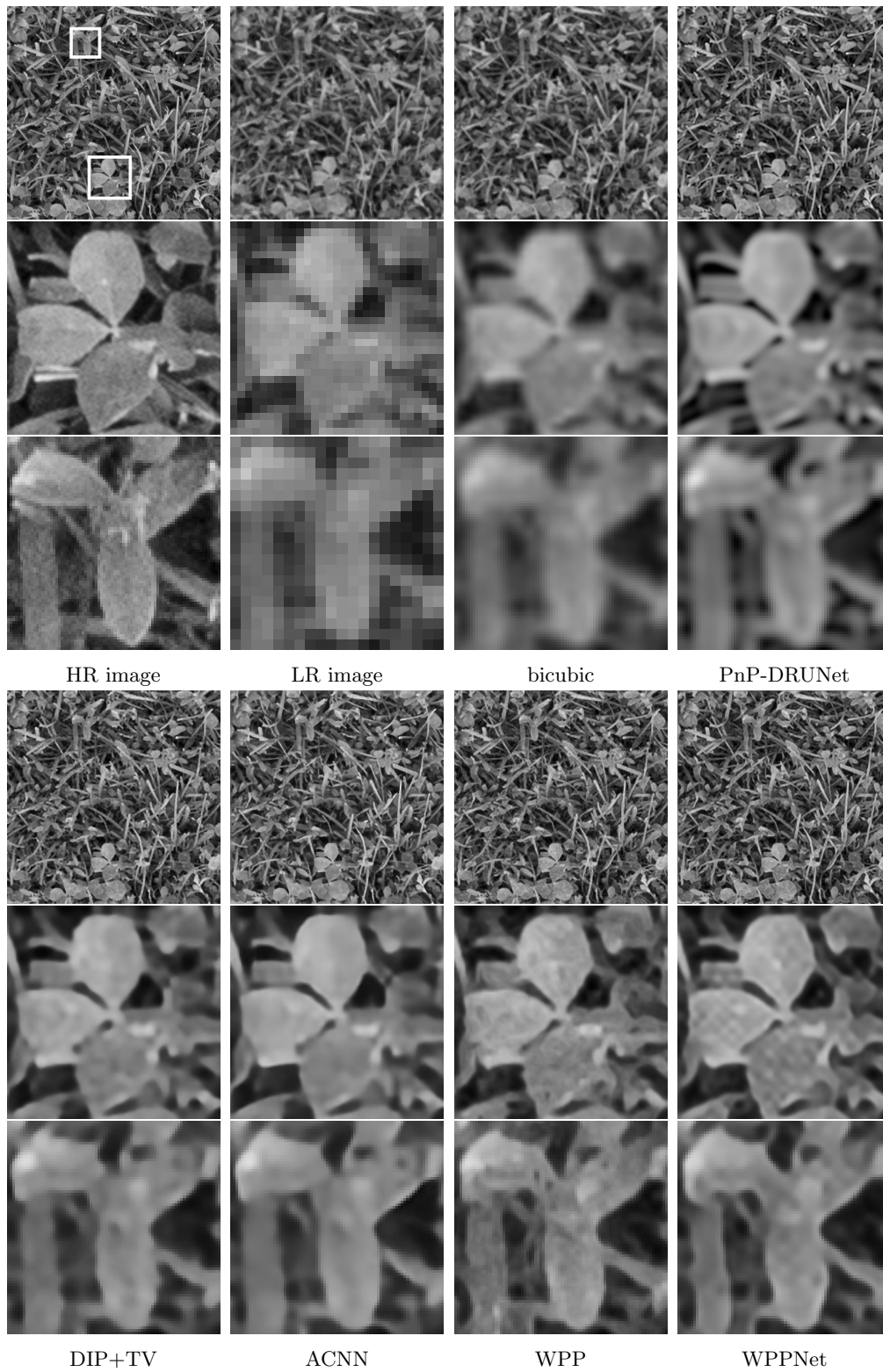


Figure 4: Comparison of superresolution for the texture “Grass” with stride 4. The zoomed-in parts are marked with a white box in the HR image.

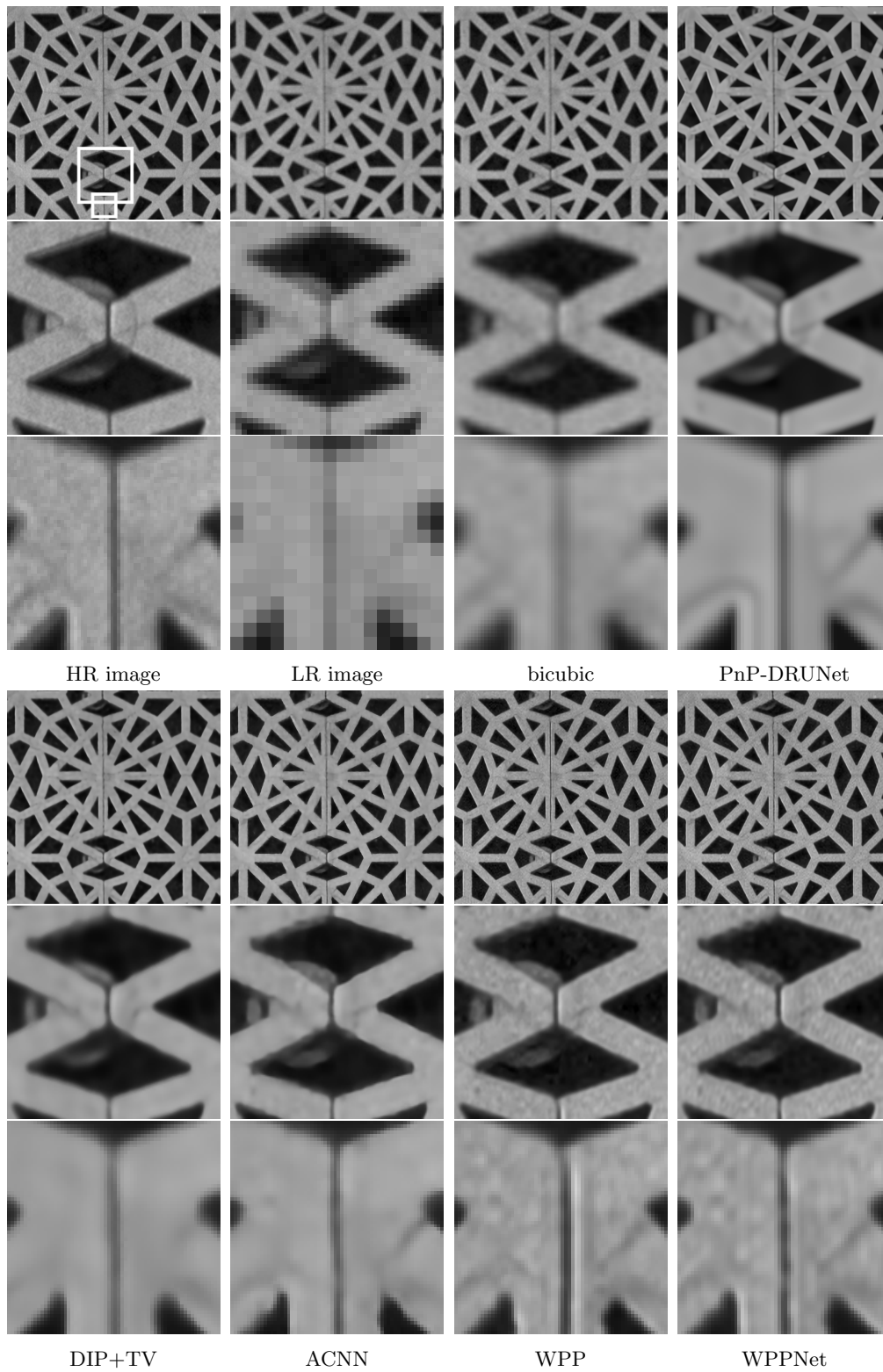


Figure 5: Comparison of superresolution for the texture “Floor” with stride 4. The zoomed-in parts are marked with a white box in the HR image.

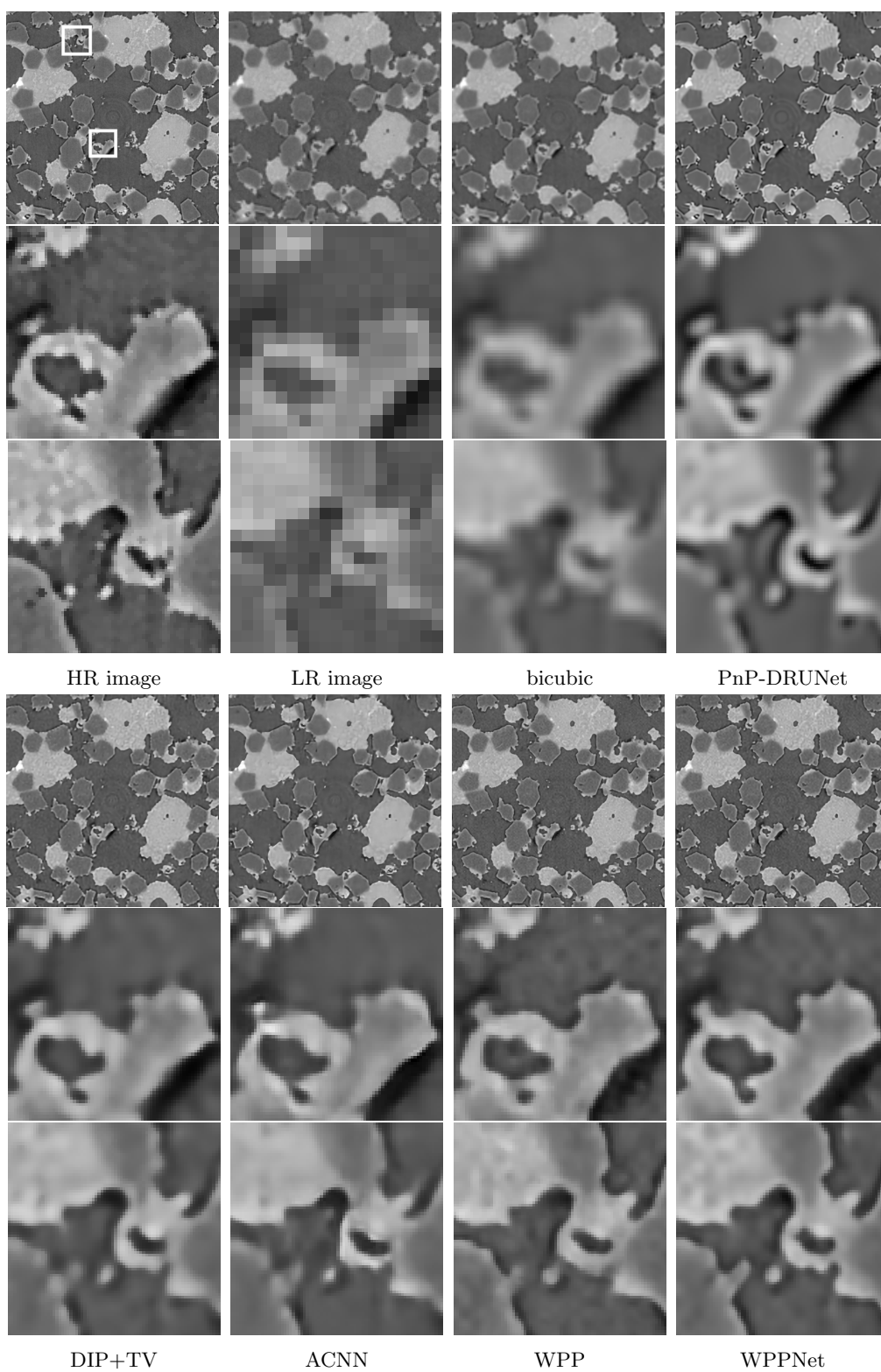


Figure 6: Comparison of superresolution for the material “SiC Diamonds” with stride 4. The zoomed-in parts are marked with a white box in the HR image.

		bicubic	PnP-DRUNet	DIP+TV	ACNN	WPP	WPPNet
SiC	PSNR	25.34	27.43	27.81	27.66	27.57	<u>27.83</u>
	Blur Effect	0.5794	0.4405	0.4046	0.4076	<u>0.3743</u>	0.3810
	LPIPS	0.4216	0.3133	0.2076	0.2441	<u>0.1627</u>	0.1819
	SSIM	0.7247	0.7770	0.7756	<u>0.7842</u>	0.7555	0.7678
	FSIM	0.8792	0.8911	0.9344	0.9130	0.9443	<u>0.9449</u>
Time	Training	-	-	-	6.5h	-	16h
	Reconstruction	0.0003s	51.36s	114.42s	0.05s	477.06s	0.05s
FS	PSNR	29.19	31.05	31.35	<u>31.68</u>	31.07	30.96
	Blur Effect	0.4856	0.4936	0.3724	0.4276	<u>0.3225</u>	0.3305
	LPIPS	0.3524	0.3565	0.2162	0.2881	<u>0.1630</u>	0.1823
	SSIM	0.7049	0.7436	0.7495	<u>0.7615</u>	0.7275	0.7297
	FSIM	0.8561	0.7888	0.9171	0.8429	0.9505	<u>0.9439</u>
Time	Training	-	-	-	6.5h	-	15h
	Reconstruction	0.0003s	51.36s	114.42s	0.05s	477.06s	0.05s

Table 2: Comparison of superresolution results for material images with stride 4. The best two values are marked in bold, the best one is additionally underlined.

5.3 Stability under Inaccurate Operators

In this subsection, we demonstrate the robustness of WPPNets against inaccurate knowledge of the forward operator f . Our data is given by the SiC Diamonds image.

5.3.1 Inaccurate Forward Operator

In this example, we generate the low-resolution observations using the forward operator f_{true} given by a strided convolution with a 16×16 Gaussian blur kernel with standard deviation 2, stride 4 and zero padding as in the previous subsection. On the other hand, we train the WPPNet and ACNN with an inaccurate forward operator f_{inacc} , which we also use for the reconstruction with DIP+TV, PnP-DRUNet and WPP. The operator f_{inacc} is given in the same way as f_{true} with the only difference, that we use a different standard deviation of 1.0, 1.5, 2.5 and 3.0.

The resulting quality measures are given in Table 4 and the reconstructions in Figure 9. We observe that WPPNet and WPP are much more robust against the inaccurate operator than all of the comparison methods. If the standard deviation of the inaccurate forward operator is smaller than the true one, we can observe a blur in the reconstructions of PnP-DRUNet, DIP+TV and ACNN, while the WPP and WPPNet reconstructions yield sharp edges. For larger standard deviations, there appear artifacts in the reconstructions of DIP+TV and ACNN, while the PnP-DRUNet reconstruction is still blurry. On the other hand, the reconstruction using WPPNet or WPP is still close to the results using the accurate

		bicubic	PnP-DRUNet	DIP+TV	ACNN	WPP	WPPNet
SiC	PSNR	22.98	24.36	<u>24.82</u>	24.20	24.51	24.44
	Blur Effect	0.6875	0.6139	0.5036	0.4476	<u>0.4081</u>	0.4151
	LPIPS	0.5988	0.4987	0.3602	0.3306	<u>0.2446</u>	0.2636
	SSIM	0.5844	0.6471	0.6500	<u>0.6515</u>	0.6488	0.6471
	FSIM	0.8371	0.8169	0.8550	0.8371	<u>0.8653</u>	0.8641
Time	Training	-	-	-	5.5h	-	28h
	Reconstruction	0.0003s	51.36s	114.42s	0.05s	477.06s	0.05s

Table 3: Comparison of superresolution results for the material ‘‘SiC’’ with stride 6. The best two values are marked in bold, the best one is additionally underlined.

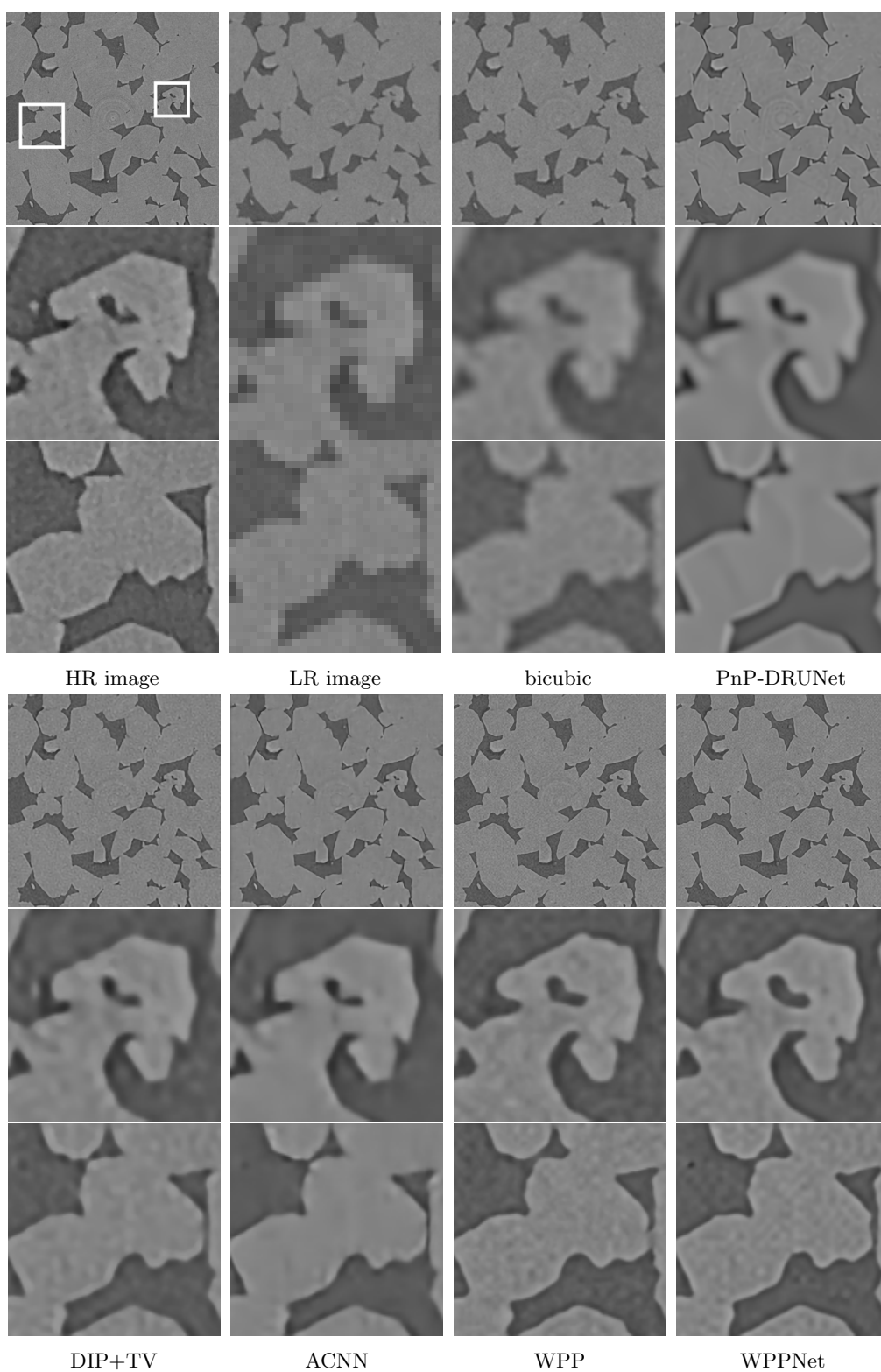


Figure 7: Comparison of superresolution for the material “FS” with stride 4. The zoomed-in parts are marked with a white box in the HR image.

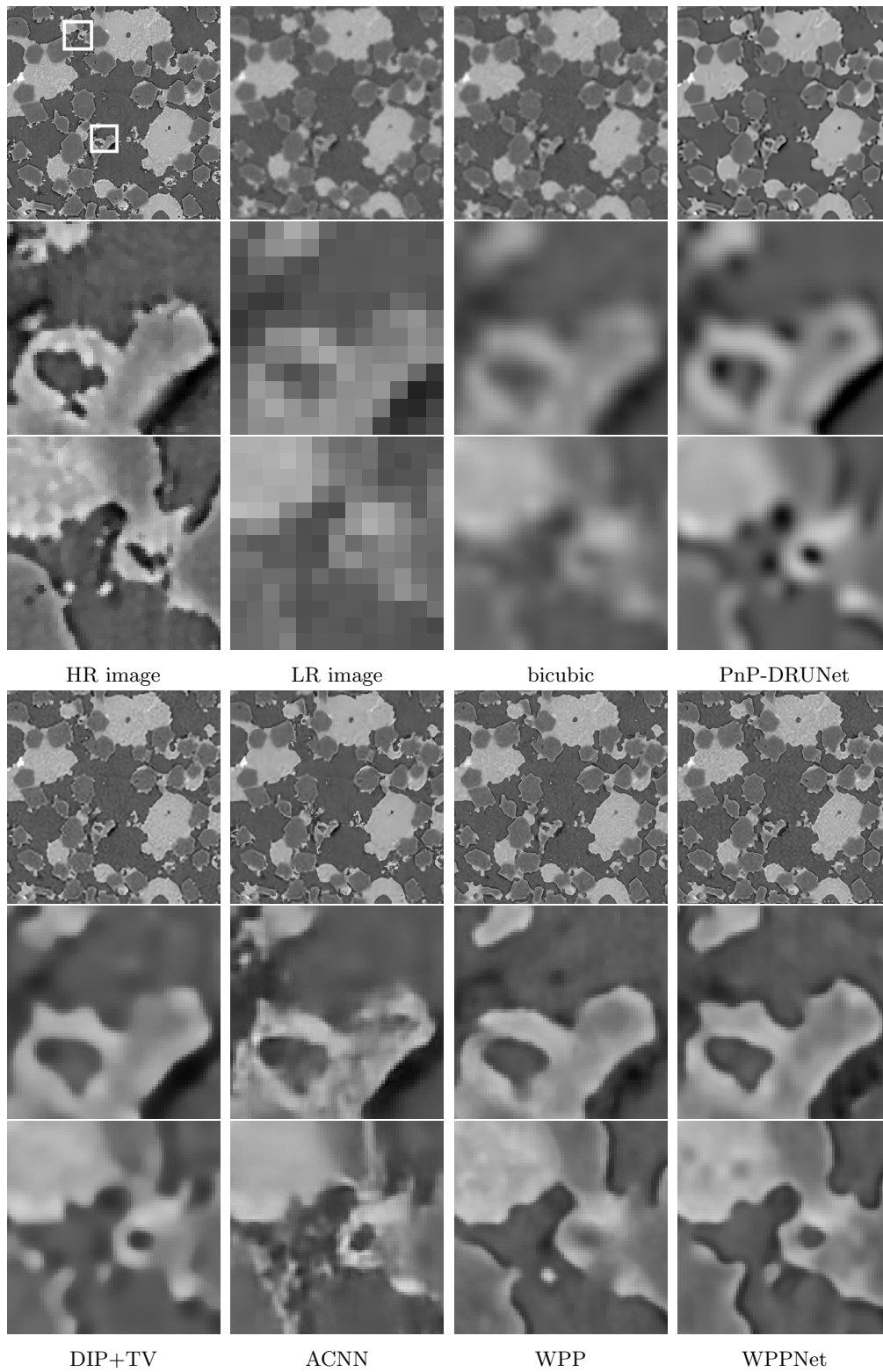


Figure 8: Comparison of superresolution for the material “SiC” with stride 6. The zoomed-in parts are marked with a white box in the HR image.

Standard deviation		PnP-DRUNet	DIP+TV	ACNN	WPP	WPPNet
1.0	PSNR	24.62	26.15	26.17	25.73	26.03
	Blur Effect	0.5769	0.4860	0.5005	0.3776	0.3841
	LPIPS	0.4511	0.2969	0.2846	0.1785	0.1862
	SSIM	0.6555	0.7347	0.7375	0.7081	0.7326
	FSIM	0.8553	0.9182	0.9074	0.9097	0.9087
Time	Training	- ⁶	-	1h	-	17h
	Reconstruction	51.36s	114.42s	0.05s	477.06s	0.05s
1.5	PSNR	26.13	26.94	26.89	26.89	27.00
	Blur Effect	0.5379	0.4631	0.4524	0.3808	0.3891
	LPIPS	0.3907	0.2639	0.2665	0.1669	0.1851
	SSIM	0.7169	0.7571	0.7613	0.7426	0.7538
	FSIM	0.8635	0.9112	0.9097	0.9345	0.9305
Time	Training	- ⁶	-	2h	-	14h
	Reconstruction	51.36s	114.42s	0.05s	477.06s	0.05s
2.0 (correct operator)	PSNR	27.43	27.81	27.66	27.57	27.83
	Blur Effect	0.4405	0.4046	0.4076	0.3743	0.3810
	LPIPS	0.3133	0.2076	0.2441	0.1627	0.1819
	SSIM	0.7770	0.7756	0.7842	0.7555	0.7678
	FSIM	0.8911	0.9344	0.9130	0.9443	0.9449
Time	Training	-	-	6.5h	-	16h
	Reconstruction	51.36s	114.42s	0.05s	477.06s	0.05s
2.5	PSNR	26.58	26.69	25.84	27.45	27.48
	Blur Effect	0.4367	0.3766	0.3445	0.3876	0.3964
	LPIPS	0.3563	0.2266	0.2420	0.1725	0.2055
	SSIM	0.7561	0.7659	0.7574	0.7617	0.7616
	FSIM	0.8751	0.9188	0.9134	0.9405	0.9411
Time	Training	- ⁶	-	2h	-	15h
	Reconstruction	51.36s	114.42s	0.05s	477.06s	0.05s
3.0	PSNR	24.99	23.52	22.34	26.73	26.91
	Blur Effect	0.4649	0.3587	0.3196	0.4117	0.4232
	LPIPS	0.4066	0.2688	0.2806	0.2011	0.2355
	SSIM	0.7049	0.7119	0.6506	0.7496	0.7539
	FSIM	0.8359	0.9014	0.9031	0.9220	0.9269
Time	Training	- ⁶	-	2h	-	12h
	Reconstruction	51.36s	114.42s	0.05s	477.06s	0.05s

Table 4: Comparison of superresolution results for “SiC” with an inaccurate forward blur operator and stride 4. The best two values are marked in bold, the best one is additionally underlined. The true forward operator has standard deviation 2.0, the values here are the same as in Table 2.

operator from the previous section. Note that for large standard deviation ACNN and DIP+TV have a very small blur effect due to the large number of high-frequency artifacts.

5.3.2 Estimated Forward Operator

Finally, we aim to evaluate the performance of WPPNets in a real-world setting motivated by the imaging of material microstructures. We assume that we have scanned a large area from a materials microstructure using a low-resolution. Due to the limited amount of time and resources it is not possible to scan the same area with a higher resolution. On the other hand, we assume that we are given a high-resolution image of some small part of this area.

In this setting, we aim to generate a high-resolution correspondence for the whole low-resolution image. We proceed in two steps. First, we estimate the forward operator of the superresolution problem using the small high-resolution part. Second, we reconstruct the high-resolution image using the estimated forward operator.

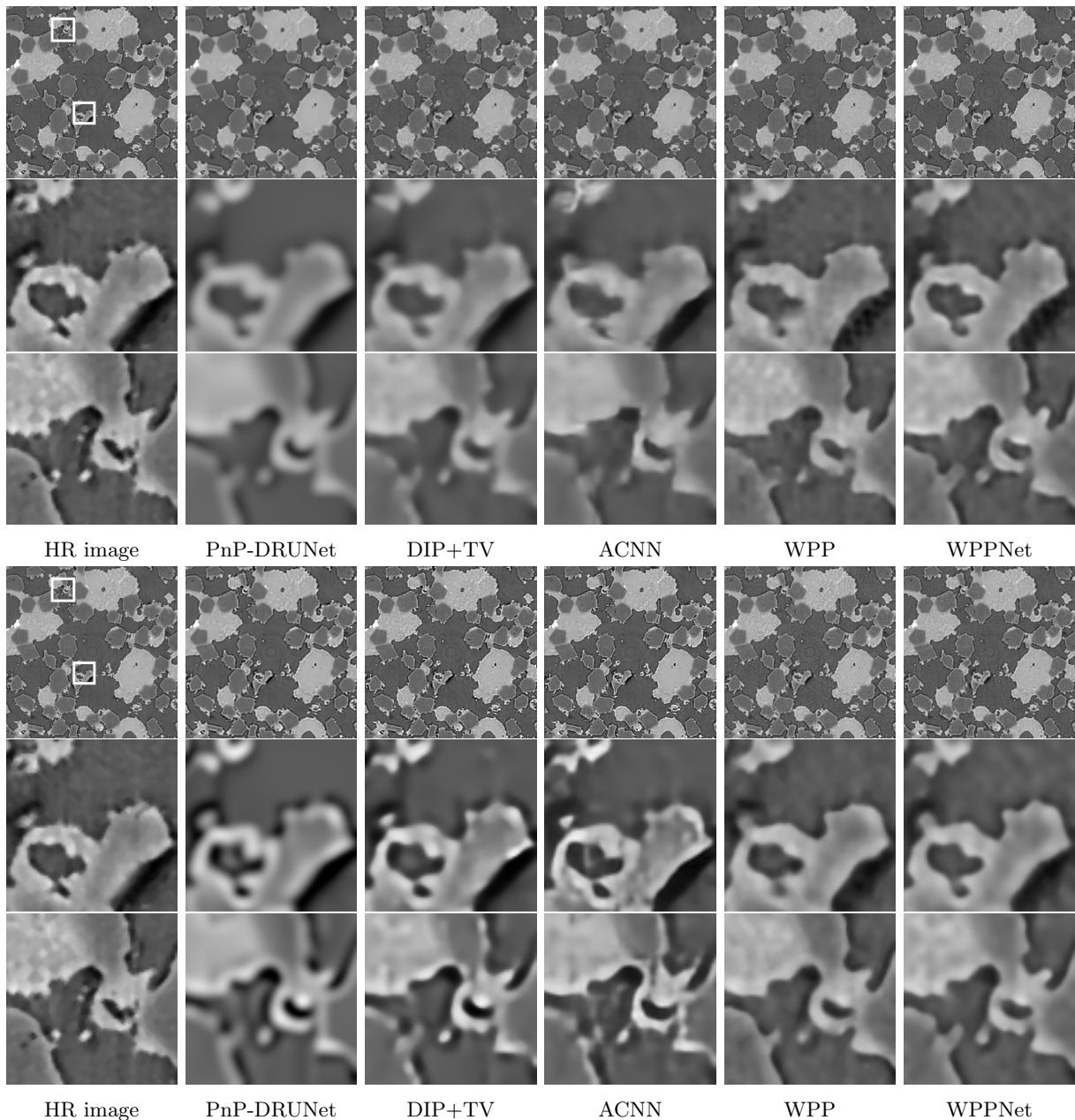


Figure 9: Comparison of superresolution for the material “SiC” with an inaccurate forward blur operator (standard deviation 1.5 (top) and 2.5 (bottom)) and stride 4. The zoomed-in parts are marked with a white box in the HR image.

Data generation and estimation of the Forward Operator Now, we consider the synchrotron-computed tomography data from Section 5.2 and consider the images with voxel spacings 1.625 μm and 3.25 μm .

Here, we extract a large database of low-resolution images (2D slices of the image with voxel spacing 3.25 μm). Further, we extract two pairs $(\tilde{x}_1, \tilde{y}_1)$ and $(\tilde{x}_2, \tilde{y}_2)$ of 2D-slices from the images with voxel spacings 1.625 μm and 3.25 μm showing the same area of the material. Here, the \tilde{x}_i are extracted from the image with voxel spacing 1.625 μm and the \tilde{y}_i come from the image with voxel spacing 3.25 μm . The

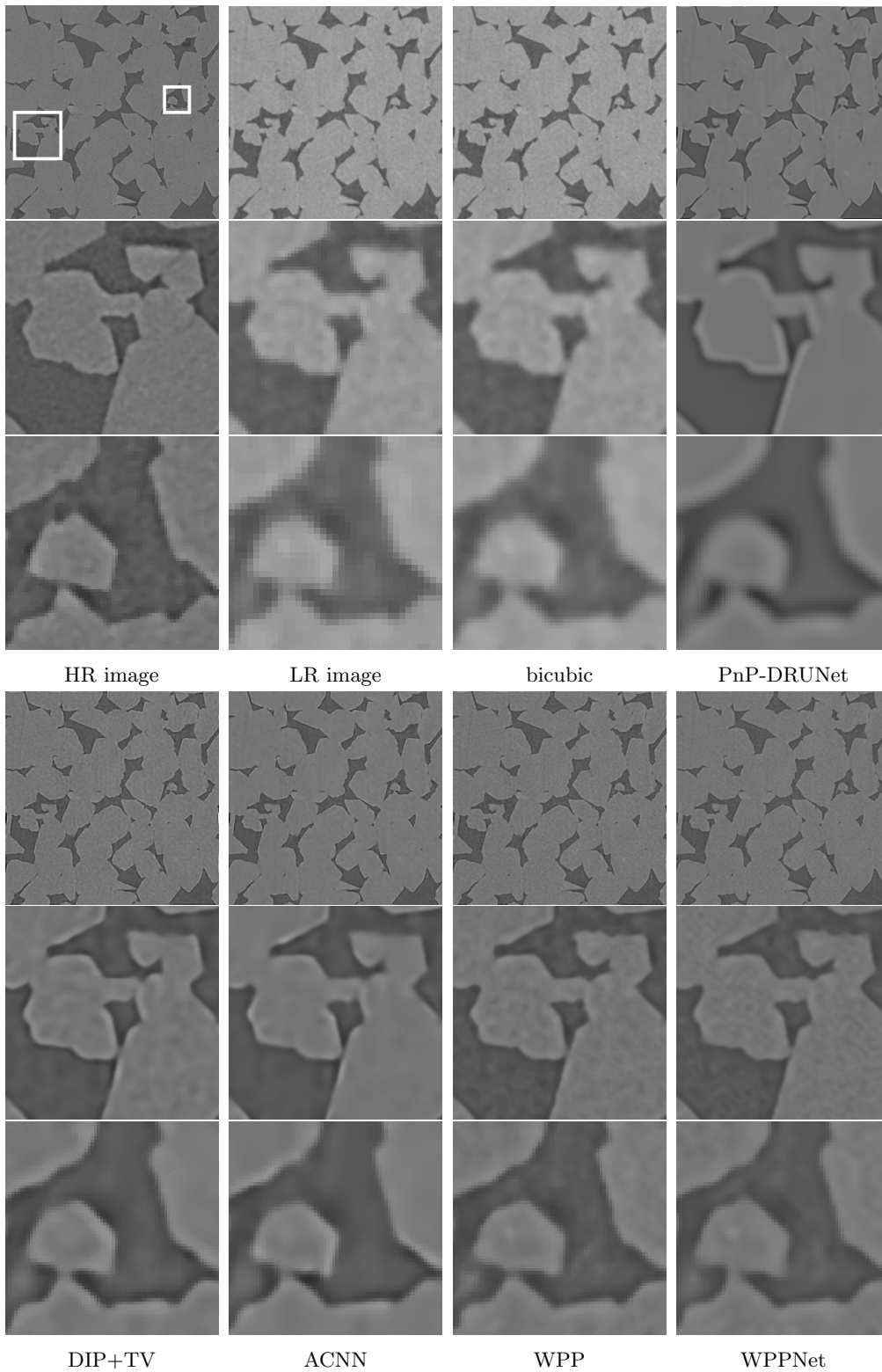


Figure 10: Reconstruction of the high-resolution image “Fontainebleau sandstone” assuming the estimated forward operator. The zoomed-in parts are marked with a white box in the HR image.

		bicubic	PnP-DRUNet	DIP +TV	ACNN	WPP	WPPNet
FS	PSNR	17.67	32.91	32.25	32.97	32.68	32.86
	Blur Effect	0.4817	0.4900	0.3900	0.4248	0.3330	0.3197
	LPIPS	0.2805	0.3442	0.2389	0.2882	0.1362	0.1411
	SSIM	0.7280	0.8151	0.7850	0.8196	0.7702	0.7724
	FSIM	0.8596	0.7903	0.8788	0.8267	0.9309	0.9365
Time	Training	-	- ⁶	-	2h	-	7h
	Reconstruction	0.0003s	51.36s	114.42s	0.05s	477.06s	0.05s

Table 5: Comparison of superresolution results using the estimated forward operator. The best two values are marked in bold, the best one is additionally underlined.

pair $(\tilde{x}_1, \tilde{y}_1)$ will be used for estimating the operator and the image \tilde{x}_1 (see Figure 2e) will serve as a reference image for WPPNet and WPP. Further, we use the pair $(\tilde{x}_2, \tilde{y}_2)$ for evaluating our results, where \tilde{y}_2 is the low-resolution observation, while \tilde{x}_2 is the high-resolution ground truth.

Note that $(\tilde{x}_i, \tilde{y}_i)$ are real-world data. Thus, we register the images $(\tilde{x}_i, \tilde{y}_i)$ in a preprocessing step using the scale-invariant feature transform (SIFT) [43].

In practice, the forward operator could also be estimated from synthetic data (see e.g., [26]), which circumvents the need of the given registered pairs $(\tilde{x}_i, \tilde{y}_i)$. However, generating synthetic data for the synchrotron-computed tomography data is out of scope of our paper.

We estimate the forward operator from the registered pair $(\tilde{x}_1, \tilde{y}_1)$ in the same way as proposed in [26]. For completeness, we describe this procedure in Appendix E.

Results The resulting quality measures are given in Table 5 and the reconstructions are shown in Figure 10. We observe that WPPNet and WPP produce significantly sharper and visually better results than the comparisons. This is also captured by the quality measures. Note, that there is a change of contrast and brightness between the high-resolution and the low-resolution image. As the bicubic interpolation does not consider the operator, this results in a brightness difference of the bicubic interpolation to the ground truth.

5.4 Uncertainty Quantification

Finally, we aim to detect the uncertainties within the reconstructions with the WPP. To this end, we consider again the SiC Diamonds images.

Magnification Factor 4 Here we use the same forward operator f as in Section 5.2, thus the same 1000 low-resolution images of size 25×25 are used for training the WPPFlow.

In Figure 11 (top) we show three different high-resolution predictions with a magnification factor 4 given the same low-resolution image. Note that here we considered the same reference image \tilde{x} as in Figure 6. We computed 100 high-resolution predictions and the resulting standard deviation is given in the right part. Here the brighter a pixel is, the less secure is the WPPFlow in its prediction; the maximal pixel-wise standard deviation is 0.08. As expected, we have a high uncertainty on the edges, while there is nearly no uncertainty in the other regions.

As a comparison, in Figure 11 (bottom) we show three different high-resolution predictions of the SRFlow. It is trained on DIV2K [1] for 1500 epochs using the negative log-likelihood which is equivalent to interchanging the two arguments within (12). The reconstructions admit a lot of artifacts and the

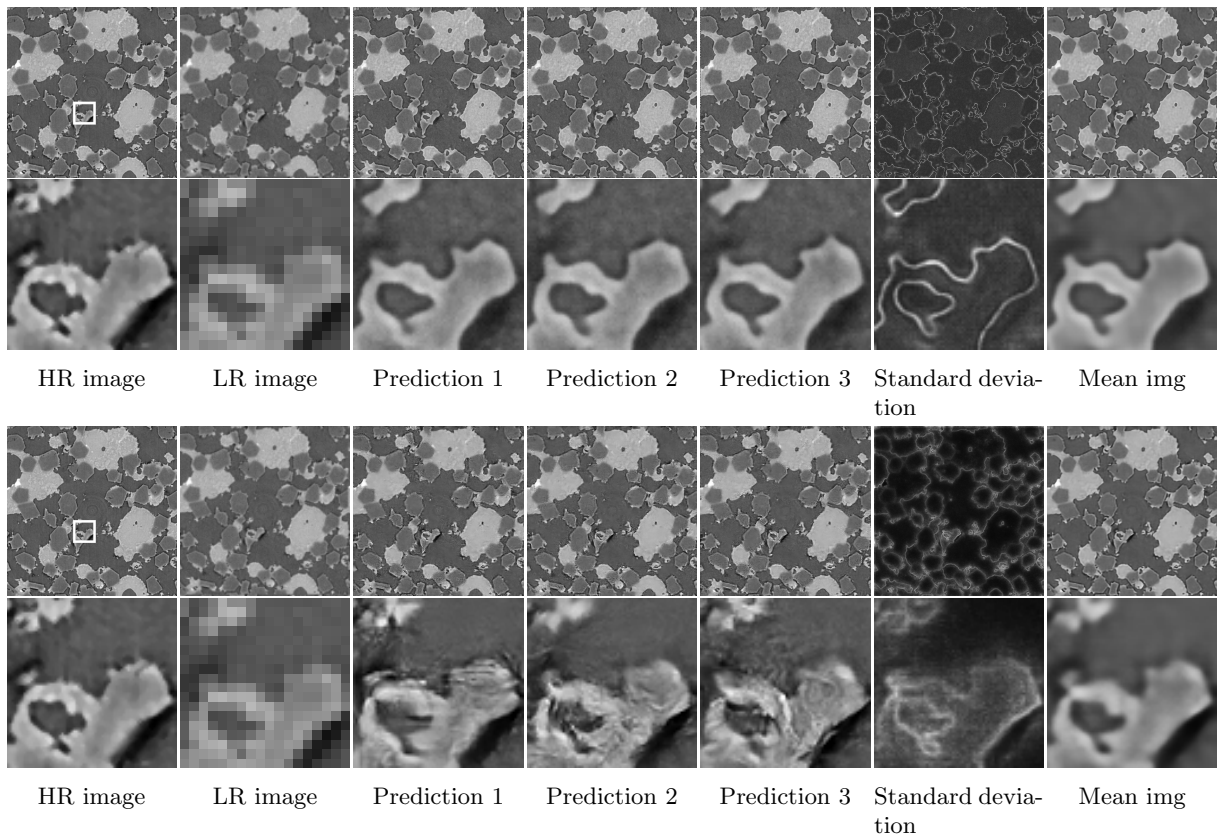


Figure 11: Different WPPFlow (top) and SRFlow (bottom) reconstructions of the ground truth image with stride 4. *Right*: The normalized standard deviation and the mean image. The zoomed-in part is marked with a white box in the HR image.

pixel-wise standard deviation is not only visible on the edges. In Figure 11 (right) we compare the mean of 100 reconstructions of WPPFlow and SRFlow. Although each reconstruction of SRFlow admits artifacts, the mean image yields a good reconstruction. This can be also seen in Table 6. Here we compare the quality measures of the mean images (left) and the averaged quality measures of the reconstructions (right). Whereas the WPPFlow reconstructions are much better, visually and in terms of the quality measures, for the mean image the SRFlow yield a better reconstruction.

Magnification Factor 8 Additionally, we consider the superresolution task with a magnification factor 8. Here, the forward operator f is given by a convolution with a 16×16 Gaussian blur kernel with standard deviation 4, stride 8 and zero-padding to keep the dimensions consistent. Again, we set the noise to $\xi \sim \mathcal{N}(0, 0.01^2)$. For training we use a generated set consisting of 270 low-resolution images of size 20×20 .

In Figure 12 (top) we show different reconstructions with a magnification factor 8 of a given low-resolution image. Of course, here the differences between the predictions are much larger and we have a higher standard deviation; the maximal pixel-wise standard deviation is 0.167. In contrast to magnification factor 4, where the uncertainties are mainly visible on the edges, in the case of magnification factor 8 the uncertainties are visible on a much larger area. In particular, we observe that WPPFlows are able to detect uncertainties in the topological structure of the data, e.g., if two certain structures are connected

		Mean img WPPFlow	Mean img SRFlow	WPPFlow	SRFlow
x4	PSNR	26.68	27.20	25.74	24.79
	Blur Effect	0.4225	0.4586	0.3539	0.3419
	LPIPS	0.2613	0.2868	0.2138	0.3090
	SSIM	0.7662	0.7642	0.6567	0.6272
	FSIM	0.9023	0.9027	0.9110	0.9064
Time	Training	-	-	25h	50h
	Reconstruction	-	-	0.06s	0.06s
x8	PSNR	23.13	23.28	21.76	19.53
	Blur Effect	0.4930	0.5977	0.3409	0.2743
	LPIPS	0.4046	0.4753	0.3495	0.4351
	SSIM	0.6281	0.5715	0.4481	0.3106
	FSIM	0.7859	0.8313	0.7687	0.7231
Time	Training	-	-	12h	42h
	Reconstruction	-	-	0.06s	0.06s

Table 6: Comparison of superresolution results using the normalizing flows. The best value is marked in bold.

or not.

In Figure 12 (bottom) we show three different high-resolution predictions of the SRFlow. It is trained on DIV2K as before for 1800 epochs. Again, the reconstructions admit a lot of artifacts and the pixel-wise standard deviation is not only visible on the edges. The mean of 100 reconstructions of WPPFlow and SRFlow is shown in Figure 12 (right). In contrast to magnification factor 4, here the mean image of the WPPFlow is visually better. For the quality measures, see again Table 6.

6 Conclusion

We introduced WPPNets, which are CNNs trained with a new loss function based on comparisons of empirical patch distributions via the quadratic Wasserstein distance and demonstrated its power by several numerical examples. In particular, we observed that WPPNets are very stable under inaccurate operators appearing in real-world applications. Due to the fact that WPPs require the knowledge of one high-resolution reference image, WPPs could also be interpreted as a method for one-shot learning, see [9, 68] and references therein. However, as no low-resolution correspondence to the reference image is given, we would call our WPP based methods an unsupervised learning method. We measured the uncertainty within the reconstructions by combining WPPs with conditional normalizing flows.

Our considerations could be extended in several directions:

- So far, we focused on image superresolution. However, the same methods can be applied for any inverse problem.
- Other noise models than the Gaussian one can be easily incorporated.
- Images of materials microstructures are often three-dimensional. Thus, in the future, we would extend the architecture of the WPPNets for three-dimensional images.
- It is desirable to establish quantitative, mathematical estimates how inaccurate operators influence the results.

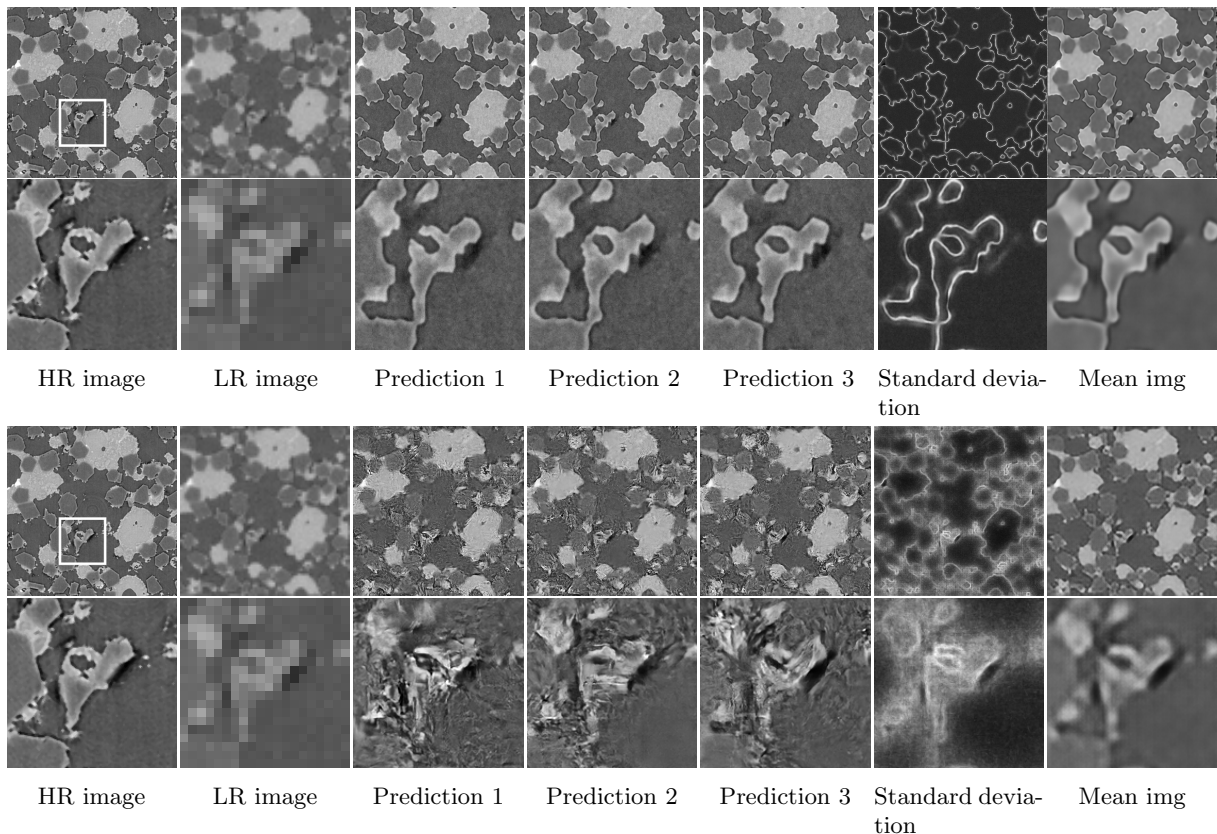


Figure 12: Different WPPFlow (top) and SRFlow (bottom) reconstructions of the ground truth image with stride 8. *Right*: The normalized standard deviation and the mean image. The zoomed-in part is marked with a white box in the HR image.

Acknowledgements

Funding by German Research Foundation (DFG) within the project STE 571/16-1 and by the DFG excellence cluster Math+ within the project TP: EF3-7 are gratefully acknowledged. The data from Section 5.2 and the second example in Section 5.3 has been acquired in the frame of the EU Horizon 2020 Marie Skłodowska-Curie Actions Innovative Training Network MUMMERING (MULTiscale, Multimodal and Multidimensional imaging for EngineeRING, Grant Number 765604) at the beamline TOMCAT of the SLS by A. Saadaldin, D. Bernard, and F. Marone Welford. We acknowledge the Paul Scherrer Institut, Villigen, Switzerland for provision of synchrotron radiation beamtime at the TOMCAT beamline X02DA of the SLS. Many thanks to Antoine Houdard for generating Figure 1 and to Dang Phoung Lan Nguyen for registering the images from the second example in Section 5.3. We would like to thank Gabriele Steidl and Paul Hagemann for fruitful discussions. Moreover, we would like to thank the anonymous reviewers for the thoughtful evaluation which helped to improve the paper.

A Proof of Proposition 5

By (4), for each $x \in \mathbb{R}^d$ it holds that

$$\begin{aligned} W_2^2(\mu_x, \mu_{\tilde{x}}) &= \max_{\psi \in \mathbb{R}^{\tilde{N}}} \left(\frac{1}{N} \sum_{j=1}^N \psi^c(P_j(x)) + \frac{1}{\tilde{N}} \sum_{k=1}^{\tilde{N}} \psi_k \right) \\ &\geq \frac{1}{N} \sum_{j=1}^N \min_{k \in \{1, \dots, \tilde{N}\}} \|P_j(x) - P_k(\tilde{x})\|_2^2, \end{aligned}$$

using $\psi = 0$. Now, for $x \in \mathbb{R}^d$ and $j \in \{1, \dots, N\}$, let $\kappa(j, x) \in \{1, \dots, \tilde{N}\}$ be one element of $\arg \min_{k \in \{1, \dots, \tilde{N}\}} (\|P_j(x) - P_k(\tilde{x})\|_2^2)$.

Moreover, let $j^*(x) \in \arg \max_{j \in \{1, \dots, N\}} \|P_j(x)\|_\infty$ be a patch which contains the entry of x with the largest absolute value. Then we have

$$\begin{aligned} W_2^2(\mu_x, \mu_{\tilde{x}}) &\geq \frac{1}{N} \sum_{j=1}^N \|P_j(x) - P_{\kappa(j,x)}(\tilde{x})\|_2^2 \\ &\geq \frac{1}{N} \|P_{j^*(x)}(x) - P_{\kappa(j^*(x),x)}(\tilde{x})\|_2^2 \\ &= \frac{1}{N} \sum_{l=1}^{p^2} ((P_{j^*(x)}(x))_l - (P_{\kappa(j^*(x),x)}(\tilde{x}))_l)^2, \end{aligned}$$

where p is the patch size. By considering just the summand l with $(P_{j^*(x)}(x))_l = \|x\|_\infty$ and using that $(P_{\kappa(j^*(x),x)}(\tilde{x}))_l \leq \|\tilde{x}\|_\infty$, we obtain

$$W_2^2(\mu_x, \mu_{\tilde{x}}) \geq \frac{1}{N} (\max(\|x\|_\infty - \|\tilde{x}\|_\infty, 0))^2 \geq \frac{1}{N} (\max(c\|x\|_2 - \|\tilde{x}\|_\infty, 0))^2,$$

for some $c > 0$. Now define the compact set $K = \{x \in \mathbb{R}^d : \|x\|_2 \leq \frac{4}{c} \|\tilde{x}\|_\infty\}$. Then, it holds for all $x \in \mathbb{R}^d \setminus K$ that

$$(\max(c\|x\|_2 - \|\tilde{x}\|_\infty, 0))^2 = (c\|x\|_2 - \|\tilde{x}\|_\infty)^2 \quad \text{and} \quad \frac{c^2}{2} \|x\|_2^2 - 2c\|x\|_2 \|\tilde{x}\|_\infty \geq 0. \quad (14)$$

We can split the integral over φ as

$$\int_{\mathbb{R}^d} |\varphi(x)| dx = \int_K |\varphi(x)| dx + \int_{\mathbb{R}^d \setminus K} |\varphi(x)| dx.$$

Since the Wasserstein distance is non-negative, we have that $|\varphi(x)| \leq 1$. As K is compact, we obtain that the first summand in the above formula is finite. It remains to show that also the second summand is finite. Indeed, it holds

$$\begin{aligned} \int_{\mathbb{R}^d \setminus K} |\varphi(x)| dx &= \int_{\mathbb{R}^d \setminus K} \exp(-\rho W_2^2(\mu_x, \mu_{\tilde{x}})) dx \\ &\leq \int_{\mathbb{R}^d \setminus K} \exp\left(-\frac{\rho}{N} (\max(c\|x\|_2 - \|\tilde{x}\|_\infty, 0))^2\right) dx \end{aligned}$$

	Figure 4	Figure 5	Figure 6	Figure 7	Figure 8	Figure 9	Figure 10
epochs	420	270	450	420	570	420	150

Table 7: Number of epochs to obtain the reconstructions visualized in the respective Figure.

Since we are integrating over all $x \in \mathbb{R}^d \setminus K$, we obtain by (14) that

$$\begin{aligned}
\int_{\mathbb{R}^d \setminus K} |\varphi(x)| dx &\leq \int_{\mathbb{R}^d \setminus K} \exp\left(-\frac{\rho}{N}(c^2\|x\|_2^2 - 2c\|x\|_2\|\tilde{x}\|_\infty + \|\tilde{x}\|_\infty^2)\right) dx \\
&\leq \int_{\mathbb{R}^d \setminus K} \exp\left(-\frac{\rho}{2N}c^2\|x\|_2^2\right) \exp\left(-\frac{\rho}{N}\underbrace{\left(\frac{c^2}{2}\|x\|_2^2 - 2c\|x\|_2\|\tilde{x}\|_\infty\right)}_{\geq 0 \text{ by (14)}}\right) dx \\
&\leq \int_{\mathbb{R}^d \setminus K} \exp\left(-\frac{\rho}{2N}c^2\|x\|_2^2\right) dx < \infty.
\end{aligned}$$

This finishes the proof. □

B Implementation details of WPPNets

All experiments are implemented in PyTorch. We run them on a single NVIDIA GeForce RTX 2060 GPU with 6 GB GPU memory.

Network Architecture We use a 16-layer CNN G_θ which is adapted from [62]. In [62] the authors propose a so-called asymmetric CNN (ACNN) for image super-resolution consisting of 23-layers. More specifically, the ACNN has a 17-layer asymmetric block, a 1-layer memory enhancement block and a 5-layer high-frequency feature enhancement block (for more details about the structure and the tasks of the individual blocks, see [62, Section III]). As stated above, we modified the proposed ACNN and take a 10-layer asymmetric block (instead of 17-layer) in order to reduce the network complexity.

Training Details For the training of the WPPNet we use the Adam optimizer [34] with a learning rate of 0.0001. The training and test data are independently chosen; we used 1000 low-resolution images of size 25×25 for training the network and have two pairs of validation images of size 600×600 and 150×150 for the high- and low-resolution image, respectively. For the training process the batch size is set to 25 and the number of epochs we trained for the reconstruction image is stated in Table 7. We choose the patch size to be $p = 6$, i.e., $P_i(x)$ is a small sub-image of size 6×6 of an image x . We subsample the number of patches in the reference image to $|I| = 10000$ accordingly to Remark 3.

To obtain an approximation of the maximizer ψ^* of F we use 20 iterations (except for Figure 4, there we used 10 iterations) of a stochastic gradient ascent with a learning rate of 1. Moreover, instead of starting with an arbitrary ψ_k^0 or choosing $\psi_k^0 = 0$ for the optimization in epoch k , we save the approximated maximizer ψ_{k-1}^{20} from the previous epoch $k-1$ and use it as the starting vector in epoch k , i.e., $\psi_{k-1}^{20} = \psi_k^0$. Herewith we reach a better approximation of the maximizer ψ_k^* in a computationally efficient way.

Hyperparameter selection As for any regularized problem the hyperparameter λ in (8) has to be chosen carefully. Since the reference image is the only given high-resolution image, we use it as a validation

image and perform a grid search of λ on it. That is, we generate a synthetic low-resolution observation of the reference image by computing $\tilde{y} = f(\tilde{x}) + \xi$ for some noise ξ and choose λ such that the reconstruction quality with respect to the PSNR of \tilde{x} from \tilde{y} is optimal.

C Implementation Details for WPPFlows

Network Architecture The conditional normalizing flow is adapted from [44]. Here the authors propose a multiscale normalizing flow with 3 and 4 scales for a magnification factor 4 and 8, respectively, consisting of 16 flow steps, followed by a transition step for learning a better transition between the scales. Moreover, as a conditioning network a standard 23-block RRDB architecture [67] is used to extract features from the given low-resolution image.

We modified the network to reduce the complexity. In particular, we do not use a conditioning network, but we use the low-resolution image itself and their bicubic interpolations for the respective scale. The input from the latent space $z \sim p_z$ is of the same size as the high-resolution reconstruction and then invertible reshaped to the size of the low-resolution. The downsample step is taken from [13], which consists of an invertible reshaping, followed by a GlowCoupling block and an Actnorm layer. Then, as in [44], 16 and 10 flow steps and a transition step follow for magnification factor 4 and 8, respectively. Lastly, a conditional affine transform in the high-resolution scale is used. Note that we do not use a splitting of 50 % in the channel dimension and we only used 2 and 3 scales for a magnification factor 4 and 8, respectively.

Training Details Similar to WPPNet, we used the Adam optimizer [34] with a learning rate of 0.0001. While 1000 low-resolution images of size 25×25 are used for training WPPFlow with a magnification factor 4, for the magnification factor 8 we used 270 low-resolution images of size 20×20 . For the training process the batch size is set to 10, the patch size is chosen to be 6 and both networks are trained for 450 epochs. We used the regularization parameter $\lambda = 100$ and the maximizer ψ^* is computed similar to WPPNets. We subsample the number of patches in the reference image to $|I| = 10000$ accordingly to Remark 3. The selection of the hyperparameter λ is done similar as for the WPPNets.

D Evaluation on a Larger Test Set

In order to make the experiments from Section 5.2 more reliable, we apply the different methods onto a larger test set. Three exemplar images from the test set are given in Figure 13. The average of the errors are given in Table 8. Again, the WPPNet and WPP perform better than the other methods in terms of the considered quality measures. Overall, the results are comparable with the results from Section 5.2.

E Estimation of the Forward Operator

In the following, we describe the estimation process of the forward operator f for superresolution, which is used in the second example of Section 5.3. For the estimation, we assume that we have given a registered pair (\tilde{x}, \tilde{y}) of a high-resolution and a low-resolution image and follow the lines of [26].

We assume that our forward operator is given by $f(x) = S(k * x + b)$ for a 15×15 blur kernel k , a bias $b \in \mathbb{R}$ and a downsampling operator S .

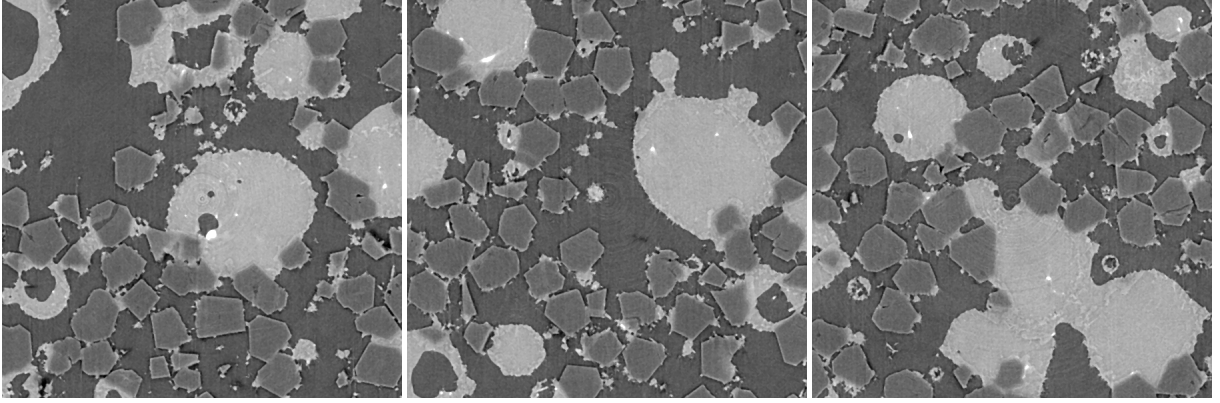


Figure 13: Exemplary ground truth images used for further numerical examples.

		bicubic	PnP-DRUNet	DIP+TV	ACNN	WPP	WPPNet
SiC	PSNR	25.70	27.72	28.04	28.00	27.73	28.00
	Blur Effect	0.5342	0.4455	0.3967	0.3783	0.3596	0.3663
	LPIPS	0.4110	0.3265	0.2141	0.2272	0.1591	0.1830
	SSIM	0.6944	0.7630	0.7677	0.7752	0.7520	0.7654
	FSIM	0.8596	0.7903	0.8788	0.8267	0.9365	0.9309

Table 8: Averaged PSNR, Blur Effect and LPIPS value of the high-resolution reconstructions. The best two values are marked in bold, the best one is additionally underlined.

Definition of the downsampling operator Further, for the downsampling operator S , we make use of Fourier transforms. Given an image $x \in \mathbb{R}^{n_x, n_y}$ the two-dimensional discrete Fourier transform (DFT) is defined by $\mathcal{F}_{n_x, n_y} := \mathcal{F}_{n_x} \otimes \mathcal{F}_{n_y}$, where we have $\mathcal{F}_n = (\exp(-2\pi ikl/n))_{k,l=0}^{n-1}$. Now, the downsampling operator $S: \mathbb{R}^{m_x, m_y} \rightarrow \mathbb{R}^{n_x, n_y}$ is given by

$$S = \frac{n_x n_y}{m_x m_y} \mathcal{F}_{n_x, n_y}^{-1} D \mathcal{F}_{m_x, m_y},$$

where for $x \in \mathbb{C}^{m_x, m_y}$ the (i, j) -th entry of $D(x)$ is given by $x_{i', j'}$, where

$$i' = \begin{cases} i, & \text{if } i \leq \frac{n_x}{2}, \\ i + m_x - n_x, & \text{otherwise.} \end{cases}$$

and j' is defined analogously. Thus, the operator S generates a downsampled version $S(x)$ of an image x by removing the high-frequency part from x . Note that even if the Fourier matrix \mathcal{F}_{n_x, n_y} is complex valued, the range of S is real-valued, as D preserves Hermitian-symmetric spectra.

Estimation of Blur Kernel and Bias We assume that we have given images $\tilde{x} \in \mathbb{R}^{m_x, m_y}$ and $\tilde{y} \in \mathbb{R}^{n_x, n_y}$ related by $\tilde{y} \approx S(k * \tilde{x} + b)$, where the blur kernel $k \in \mathbb{R}^{15 \times 15}$ and the bias $b \in \mathbb{R}$ are unknown. In the following, we aim to reconstruct k and b from \tilde{x} and \tilde{y} . Here, we use the notations $N = n_x n_y$ and $M = m_x m_y$. Further let $\tilde{k} \in \mathbb{R}^{m_x, m_y}$ be the kernel k padded with zeros such that it still corresponds to the same convolution as k , but has size $m_x \times m_y$.

Applying the DFT on both sides of $y = S(k * \tilde{x} + b) = S(\tilde{k} * \tilde{x} + b)$ and using the definition of S , we

obtain that

$$\hat{y} = \frac{N}{M}D(\hat{k} \odot \hat{x} + Mbe) = \frac{N}{M}D(\hat{k}) \odot D(\hat{x}) + Nbe,$$

where $\hat{y} = \mathcal{F}_{n_x, n_y} \tilde{y}$, $\hat{x} = \mathcal{F}_{m_x, m_y} \tilde{x}$, $\hat{k} = \mathcal{F}_{m_x, m_y} \tilde{k}$, \odot is the elementwise product and e denotes the first unit vector (i.e., $e_{0,0} = 1$ and all other entries are zero). Now, we can conclude that

$$D(\hat{k}) = \frac{M}{N}\hat{y} \oslash D(\hat{x}) - \frac{Mb}{\hat{x}_{0,0}}e,$$

where \oslash is the elementwise quotient. In practice, we stabilize this quotient by increasing the absolute value of $D(\hat{x})$ by 10^{-5} while retaining the phase. Thus, assuming that the high-frequency part of k is negligible (i.e., that $D^T Dk = k$), we can approximate \hat{k} by

$$\hat{k} \approx \frac{M}{N}D^T \hat{y} \oslash D(\hat{x}) - \frac{Mb}{\hat{x}_{0,0}}e.$$

Applying the inverse DFT this becomes

$$\tilde{k} \approx \mathcal{F}_{m_x, m_y}^{-1} \left(\frac{M}{N}D^T(\hat{y} \oslash D(\hat{x})) \right) - \frac{b}{\hat{x}_{0,0}}.$$

Using the assumption that \tilde{k} is zero outside of the 15×15 patch, where k is located, we can estimate b by taking the mean over all pixels of $\mathcal{F}_{m_x, m_y}^{-1} \left(\frac{M}{N}D^T(\hat{y} \oslash D(\hat{x})) \right)$ outside of this 15×15 patch. Afterwards, we estimate k by reprojecting

$$\mathcal{F}_{m_x, m_y}^{-1} \left(\frac{M}{N}D^T(\hat{y} \oslash D(\hat{x})) \right) - \frac{b}{\hat{x}_{0,0}}$$

to the set of all real 15×15 kernels.

References

- [1] E. Agustsson and R. Timofte. Ntire 2017 challenge on single image super-resolution: Dataset and study. In *The IEEE Conference on Computer Vision and Pattern Recognition (CVPR) Workshops*, July 2017.
- [2] A. Andrieu, N. Farchmin, P. Hagemann, S. Heidenreich, V. Soltwisch, and G. Steidl. Invertible neural networks versus MCMC for posterior reconstruction in grazing incidence X-ray fluorescence. In *International Conference on Scale Space and Variational Methods in Computer Vision*, pages 528–539. Springer, 2021.
- [3] L. Ardizzone, J. Kruse, C. Lüth, N. Bracher, C. Rother, and U. Köthe. Conditional invertible neural networks for diverse image-to-image translation. In *Pattern Recognition: 42nd DAGM German Conference, DAGM GCPR 2020, Tübingen, Germany, September 28 – October 1, 2020, Proceedings*, page 373–387, Berlin, Heidelberg, 2020. Springer-Verlag.
- [4] L. Ardizzone, J. Kruse, C. Rother, and U. Köthe. Analyzing inverse problems with invertible neural networks. In *7th International Conference on Learning Representations, ICLR 2019, New Orleans, LA, USA, May 6-9, 2019*, 2019.

- [5] D. O. Bagger, J. Leuschner, and M. Schmidt. Computed tomography reconstruction using deep image prior and learned reconstruction methods. *Inverse Problems*, 36, 2020.
- [6] A. Buades, B. Coll, and J.-M. Morel. A non-local algorithm for image denoising. In *2005 IEEE Computer Society Conference on Computer Vision and Pattern Recognition*, volume 2, pages 60–65. IEEE, 2005.
- [7] S. H. Chan, X. Wang, and O. A. Elgendy. Plug-and-play ADMM for image restoration: Fixed-point convergence and applications. *IEEE Transactions on Computational Imaging*, 3(1):84–98, 2016.
- [8] R. Chen, J. Behrmann, D. K. Duvenaud, and J.-H. Jacobsen. Residual flows for invertible generative modeling. In *Advances in Neural Information Processing Systems*, volume 32. Curran Associates, Inc., 2019.
- [9] J. Cheng, Z. Han, Z. Wang, and L. Chen. “One-shot” super-resolution via backward style transfer for fast high-resolution style transfer. *IEEE Signal Processing Letters*, 28:1485–1489, 2021.
- [10] P. L. Combettes and V. R. Wajs. Signal recovery by proximal forward-backward splitting. *Multiscale Modeling & Simulation*, 4(4):1168–1200, 2005.
- [11] L. Condat, D. Kitahara, A. Contreras, and A. Hirabayashi. Proximal splitting algorithms: Relax them all. *arXiv preprint arXiv:1912.00137*, 2019.
- [12] F. Crete, T. Dolmiere, P. Ladret, and M. Nicolas. The blur effect: perception and estimation with a new no-reference perceptual blur metric. In *Human vision and electronic imaging XII*, volume 6492, page 64920I. International Society for Optics and Photonics, 2007.
- [13] A. Denker, M. Schmidt, J. Leuschner, and P. Maass. Conditional invertible neural networks for medical imaging. *Journal of Imaging*, 7(11), 2021.
- [14] L. Dinh, J. Sohl-Dickstein, and S. Bengio. Density estimation using real NVP. In *5th International Conference on Learning Representations, ICLR 2017, Toulon, France, April 24-26, 2017, Conference Track Proceedings*, 2017.
- [15] C. Dong, C. C. Loy, K. He, and X. Tang. Image super-resolution using deep convolutional networks. *IEEE Transactions on Pattern Analysis and Machine Intelligence*, 38(2):295–307, 2015.
- [16] J. Eckstein and D. P. Bertsekas. On the Douglas—Rachford splitting method and the proximal point algorithm for maximal monotone operators. *Mathematical Programming*, 55(1):293–318, 1992.
- [17] A. Effland, E. Kobler, K. Kunisch, and T. Pock. Variational networks: An optimal control approach to early stopping variational methods for image restoration. *Journal of Mathematical Imaging and Vision*, 62(3):396, 2020.
- [18] A. A. Efros and T. K. Leung. Texture synthesis by non-parametric sampling. In *Proceedings of the seventh IEEE International Conference on Computer Vision*, volume 2, pages 1033–1038. IEEE, 1999.
- [19] C. Etmann, R. Ke, and C.-B. Schönlieb. iunets: learnable invertible up-and downsampling for large-scale inverse problems. In *2020 IEEE 30th International Workshop on Machine Learning for Signal Processing (MLSP)*, pages 1–6. IEEE, 2020.

- [20] R. Friedman and Y. Weiss. Posterior sampling for image restoration using explicit patch priors. *arXiv preprint arXiv:2104.09895*, 2021.
- [21] K. Gregor and Y. LeCun. Learning fast approximations of sparse coding. In *Proceedings of the 27th international conference on international conference on machine learning*, pages 399–406, 2010.
- [22] H. Gupta, K. H. Jin, H. Q. Nguyen, M. T. McCann, and M. Unser. CNN-based projected gradient descent for consistent CT image reconstruction. *IEEE Transactions on Medical Imaging*, 37(6):1440–1453, 2018.
- [23] J. Gutierrez, J. Rabin, B. Galerne, and T. Hurtut. Optimal patch assignment for statistically constrained texture synthesis. In *International Conference on Scale Space and Variational Methods in Computer Vision*, pages 172–183. Springer, 2017.
- [24] P. Hagemann, J. Hertrich, and G. Steidl. Generalized normalizing flows via Markov chains. *arXiv preprint arXiv:2111.12506*, 2021.
- [25] P. Hagemann, J. Hertrich, and G. Steidl. Stochastic normalizing flows for inverse problems: A Markov chains viewpoint. *SIAM/ASA Journal on Uncertainty Quantification*, 10(3):1162–1190, 2022.
- [26] J. Hertrich, A. Houdard, and C. Redenbach. Wasserstein patch prior for image superresolution. *IEEE Transactions on Computational Imaging*, 8:693–704, 2022.
- [27] J. Hertrich, S. Neumayer, and G. Steidl. Convolutional proximal neural networks and plug-and-play algorithms. *Linear Algebra and its Applications*, 631:203–234, 2021.
- [28] J. Hertrich, D. P. L. Nguyen, J.-F. Aujol, D. Bernard, Y. Berthoumieu, A. Saadaldin, and G. Steidl. PCA reduced Gaussian mixture models with applications in superresolution. *Inverse Problems & Imaging*, 2021.
- [29] A. Houdard, C. Bouveyron, and J. Delon. High-dimensional mixture models for unsupervised image denoising (HDMI). *SIAM Journal on Imaging Sciences*, 11(4):2815–2846, 2018.
- [30] A. Houdard, A. Leclaire, N. Papadakis, and J. Rabin. Wasserstein generative models for patch-based texture synthesis. In A. Elmoataz, J. Fadili, Y. Quéau, J. Rabin, and L. Simon, editors, *Scale Space and Variational Methods in Computer Vision*, page 269–280, Cham, 2021. Springer International Publishing.
- [31] A. Houdard, A. Leclaire, N. Papadakis, and J. Rabin. A generative model for texture synthesis based on optimal transport between feature distributions. *Journal of Mathematical Imaging and Vision*, 2022.
- [32] M. Jiu and N. Pustelnik. A deep primal-dual proximal network for image restoration. *IEEE Journal of Selected Topics in Signal Processing*, 15(2):190–203, 2021.
- [33] R. Keys. Cubic convolution interpolation for digital image processing. *IEEE Transactions on Acoustics, Speech, and Signal Processing*, 29(6):1153–1160, 1981.
- [34] D. P. Kingma and J. Ba. Adam: A method for stochastic optimization. In *International Conference on Learning Representations*, 2015.

- [35] D. P. Kingma and P. Dhariwal. Glow: Generative flow with invertible 1x1 convolutions. *Advances in neural information processing systems*, 31, 2018.
- [36] E. Kobler, A. Effland, K. Kunisch, and T. Pock. Total deep variation for linear inverse problems. In *Proceedings of the IEEE/CVF Conference on Computer Vision and Pattern Recognition*, pages 7549–7558, 2020.
- [37] J. Kruse, G. Detommaso, R. Scheichl, and U. Köthe. Hint: Hierarchical invertible neural transport for density estimation and bayesian inference. *arXiv preprint arXiv:1905.10687v1*, 2019.
- [38] G. Kylberg. *The Kylberg texture dataset v. 1.0*. Centre for Image Analysis, Swedish University of Agricultural Sciences and Uppsala University, 2011.
- [39] M. Lebrun, A. Buades, and J.-M. Morel. A nonlocal Bayesian image denoising algorithm. *SIAM Journal on Imaging Sciences*, 6(3):1665–1688, 2013.
- [40] A. Leclaire and J. Rabin. A fast multi-layer approximation to semi-discrete optimal transport. In *International Conference on Scale Space and Variational Methods in Computer Vision*, pages 341–353. Springer, 2019.
- [41] C. Ledig, L. Theis, F. Huszár, J. Caballero, A. Cunningham, A. Acosta, A. Aitken, A. Tejani, J. Totz, Z. Wang, et al. Photo-realistic single image super-resolution using a generative adversarial network. In *Proceedings of the IEEE conference on computer vision and pattern recognition*, pages 4681–4690, 2017.
- [42] B. Lim, S. Son, H. Kim, S. Nah, and K. Mu Lee. Enhanced deep residual networks for single image super-resolution. In *Proceedings of the IEEE Conference on Computer Vision and Pattern Recognition workshops*, pages 136–144, 2017.
- [43] D. G. Lowe. Object recognition from local scale-invariant features. In *Proceedings of the seventh IEEE International Conference on Computer Vision*, volume 2, pages 1150–1157. IEEE, 1999.
- [44] A. Lugmayr, M. Danelljan, L. Van Gool, and R. Timofte. SRFlow: Learning the super-resolution space with normalizing flow. In *ECCV*, 2020.
- [45] B. Malézieux, T. Moreau, and M. Kowalski. Understanding approximate and unrolled dictionary learning for pattern recovery. In *International Conference on Learning Representations*, 2021.
- [46] D. Martin, C. Fowlkes, D. Tal, and J. Malik. A database of human segmented natural images and its application to evaluating segmentation algorithms and measuring ecological statistics. In *Proceedings of the International Conference on Computer Vision*, volume 2, pages 416–423, July 2001.
- [47] T. Meinhardt, M. Moller, C. Hazirbas, and D. Cremers. Learning proximal operators: Using denoising networks for regularizing inverse imaging problems. In *Proceedings of the IEEE International Conference on Computer Vision*, pages 1781–1790, 2017.
- [48] S. Ono. Primal-dual plug-and-play image restoration. *IEEE Signal Processing Letters*, 24(8):1108–1112, 2017.

- [49] S. Parameswaran, C. Deledalle, L. Denis, and T. Q. Nguyen. Accelerating GMM-based patch priors for image restoration: Three ingredients for a 100x speed-up. *IEEE Transactions on Image Processing*, 28(2):687–698, 2019.
- [50] T. Pinetz, E. Kobler, T. Pock, and A. Effland. Shared prior learning of energy-based models for image reconstruction. *SIAM Journal on Imaging Sciences*, 14(4):1706–1748, 2021.
- [51] J. Rabin, G. Peyré, J. Delon, and M. Bernot. Wasserstein barycenter and its application to texture mixing. In *International Conference on Scale Space and Variational Methods in Computer Vision*, pages 435–446. Springer, 2011.
- [52] D. Rezende and S. Mohamed. Variational inference with normalizing flows. In *International conference on machine learning*, pages 1530–1538. PMLR, 2015.
- [53] G. O. Roberts and J. S. Rosenthal. General state space markov chains and mcmc algorithms. *Probability surveys*, 1:20–71, 2004.
- [54] Y. Romano, M. Elad, and P. Milanfar. The little engine that could: Regularization by denoising (RED). *SIAM Journal on Imaging Sciences*, 10(4):1804–1844, 2017.
- [55] Y. Romano, J. Isidoro, and P. Milanfar. RAISR: Rapid and accurate image super resolution. *IEEE Transactions on Computational Imaging*, 3(1):110–125, 2017.
- [56] C. Saharia, J. Ho, W. Chan, T. Salimans, D. J. Fleet, and M. Norouzi. Image super-resolution via iterative refinement. *IEEE Transactions on Pattern Analysis and Machine Intelligence*, 2022.
- [57] P. Sandeep and T. Jacob. Single image super-resolution using a joint GMM method. *IEEE Transactions on Image Processing*, 25(9):4233–4244, 2016.
- [58] F. Santambrogio. *Optimal Transport for Applied Mathematicians : Calculus of Variations, PDEs, and Modeling*. Progress in nonlinear differential equations and their applications. Birkhäuser, Cham, 2015.
- [59] H. Shi, Y. Traonmilin, and J.-F. Aujol. Compressive learning for patch-based image denoising. *SIAM Journal on Imaging Sciences*, 15(3):1184–1212, 2022.
- [60] A. Shocher, N. Cohen, and M. Irani. “Zero-shot” super-resolution using deep internal learning. In *Proceedings of the IEEE Conference on Computer Vision and Pattern Recognition*, pages 3118–3126, 2018.
- [61] H. Sun and K. L. Bouman. Deep probabilistic imaging: Uncertainty quantification and multi-modal solution characterization for computational imaging. In *Proceedings of the AAAI Conference on Artificial Intelligence*, volume 35, pages 2628–2637, 2021.
- [62] C. Tian, Y. Xu, W. Zuo, C.-W. Lin, and D. Zhang. Asymmetric CNN for image superresolution. *IEEE Transactions on Systems, Man, and Cybernetics: Systems*, 2021.
- [63] D. Ulyanov, A. Vedaldi, and V. Lempitsky. Deep image prior. In *Proceedings of the IEEE Conference on Computer Vision and Pattern Recognition*, pages 9446–9454, 2018.

- [64] S. Vaucher, P. Unifantowicz, C. Ricard, L. Dubois, M. Kuball, J.-M. Catala-Civera, D. Bernard, M. Stampanoni, and R. Nicula. On-line tools for microscopic and macroscopic monitoring of microwave processing. *Physica B: Condensed Matter*, 398(2):191–195, 2007.
- [65] S. V. Venkatakrisnan, C. A. Bouman, and B. Wohlberg. Plug-and-play priors for model based reconstruction. In *2013 IEEE Global Conference on Signal and Information Processing*, pages 945–948. IEEE, 2013.
- [66] X. Wang, K. Yu, S. Wu, J. Gu, Y. Liu, C. Dong, Y. Qiao, and C. Change Loy. ESRGAN: Enhanced super-resolution generative adversarial networks. In *Proceedings of the European Conference on Computer Vision (ECCV) workshops*, pages 0–0, 2018.
- [67] X. Wang, K. Yu, S. Wu, J. Gu, Y. Liu, C. Dong, Y. Qiao, and C. C. Loy. Esrgan: Enhanced super-resolution generative adversarial networks. In L. Leal-Taixé and S. Roth, editors, *Computer Vision – ECCV 2018 Workshops*, pages 63–79, Cham, 2019. Springer International Publishing.
- [68] Y. Wang, Q. Yao, J. T. Kwok, and L. M. Ni. Generalizing from a few examples: A survey on few-shot learning. *ACM Computing Surveys*, 53(3), 2020.
- [69] Z. Wang, A. Bovik, H. Sheikh, and E. Simoncelli. Image quality assessment: From error visibility to structural similarity. *IEEE Transactions on Image Processing*, 13(4):600–612, 2004.
- [70] Z. Wang, J. Chen, and S. C. Hoi. Deep learning for image super-resolution: A survey. *IEEE Transactions on Pattern Analysis and Machine Intelligence*, 2020.
- [71] K. Zhang, Y. Li, W. Zuo, L. Zhang, L. Van Gool, and R. Timofte. Plug-and-play image restoration with deep denoiser prior. *IEEE Transactions on Pattern Analysis and Machine Intelligence*, 2021.
- [72] L. Zhang, L. Zhang, X. Mou, and D. Zhang. FSIM: A feature similarity index for image quality assessment. *IEEE Transactions on Image Processing*, 20(8):2378–2386, 2011.
- [73] R. Zhang, P. Isola, A. A. Efros, E. Shechtman, and O. Wang. The unreasonable effectiveness of deep features as a perceptual metric. In *Proceedings of the IEEE Conference on Computer Vision and Pattern Recognition*, pages 586–595, 2018.
- [74] Y. Zhang, Y. Tian, Y. Kong, B. Zhong, and Y. Fu. Residual dense network for image super-resolution. In *Proceedings of the IEEE Conference on Computer Vision and Pattern Recognition*, pages 2472–2481, 2018.
- [75] D. Zoran and Y. Weiss. From learning models of natural image patches to whole image restoration. In *IEEE International Conference on Computer Vision*, pages 479–486. IEEE, 2011.